Palaeogeography, Palaeoclimatology, Palaeoecology 498 (2018) 53–67

Contents lists available at ScienceDirect

Palaeogeography, Palaeoclimatology, Palaeoecology

journal homepage: www.elsevier.com/locate/palaeo

Climate stability in central Anatolia during the Messinian Salinity Crisis

Maud J.M. Meijers[a,b,*], A. Ahmet Peynircioğlu[c], Michael A. Cosca[d], Gilles Y. Brocard[e,f], Donna L. Whitney[b], Cor G. Langereis[c], Andreas Mulch[a,g]

[a] Senckenberg Biodiversity and Climate Research Centre (BiK-F), Frankfurt, Germany
[b] Department of Earth Sciences, University of Minnesota, Minneapolis, MN, USA
[c] Paleomagnetic laboratory 'Fort Hoofddijk', Utrecht University, Netherlands
[d] U.S. Geological Survey, Denver, CO, USA
[e] Department of Earth and Environmental Sciences, University of Pennsylvania, Philadelphia, USA
[f] School of Geosciences, The University of Sydney, Australia
[g] Institute of Geosciences, Goethe University Frankfurt, Frankfurt, Germany

ARTICLE INFO

Keywords:
Central Anatolian Plateau
Magnetostratigraphy
Stable isotope geochemistry
Messinian Salinity Crisis
Continental sedimentation

ABSTRACT

Deposition of large amounts of evaporites and erosion of deep canyons within the Mediterranean Basin as a result of reduced basin connectivity with the Atlantic Ocean and the epicontinental Paratethys Sea characterized the Messinian Salinity Crisis (MSC, 5.97–5.33 Ma). The influence of the MSC on Mediterranean environmental conditions within the basin itself has been intensely studied from marine records, but reconstructing the impact of the MSC on circum-Mediterranean continental climate has been hampered by the absence of continuous sedimentary archives that span the duration of the event.

Here, we report results of a continental record of carbon ($\delta^{13}C$) and oxygen ($\delta^{18}O$) isotopes from lake carbonates framed by new magnetostratigraphic and $^{40}Ar/^{39}Ar$ dating, as well as by existing mammal stratigraphy (Kangal Basin, central Anatolia). The sampled section records continuous fluvio-lacustrine sedimentation from ~6.6 Ma to 4.9 Ma, which spans the MSC and the Miocene-Pliocene boundary. This dataset so far represents the only continuous continental paleoenvironmental record of the MSC in the circum-Mediterranean realm.

The Kangal Basin isotope record indicates a low degree of evaporation. Furthermore, covariance between $\delta^{13}C$ and $\delta^{18}O$ suggests a coupling between lake water balance and biologic productivity. Variations in $\delta^{13}C$ and $\delta^{18}O$ therefore likely reflect changes in the amount of incoming precipitation, rather than changes in $\delta^{18}O$ values of incoming precipitation. The most prominent spike in $\delta^{13}C$ and $\delta^{18}O$ occurs during the acme of the MSC and is therefore interpreted to have resulted from a decrease in the amount of incoming moisture correlative to a period of vigorous erosion and sea level lowering in the Mediterranean Basin. Major sea level lowering of Mediterranean basin waters during the acme of the MSC could have therefore led to slightly dryer conditions over Anatolia, which is also suggested by modeling studies. Overall, changes in $\delta^{13}C$ and $\delta^{18}O$ values are small. Therefore, we surmise that the MSC had limited effects on the paleoenvironmental and paleoclimatic conditions in the Anatolian interior.

1. Introduction

Periods of restricted connectivity between the Mediterranean Sea and the Atlantic Ocean, as well as with the large epicontinental Paratethys Sea, characterized the Mediterranean region during the Messinian Salinity Crisis (MSC, 5.97–5.33 Ma; Fig. 1). The epicontinental Paratethys Sea stretched from the Carpathians to the Caspian Sea via the Black Sea from the middle Miocene to the (early) Pliocene (e.g. Krijgsman et al., 2010). Between 5.60 and 5.55 Ma the MSC culminated in halite precipitation within the Mediterranean Basin and incision of deep canyons along its margins (Hsü et al., 1973; Rouchy and Caruso, 2006). Numerous brackish-marine sediment occurrences document the dramatic paleoenvironmental changes that accompanied the MSC sea level fluctuations. Whereas the impact of these large-magnitude changes in sea level provided detailed insight into Mediterranean Basin dynamics and paleoenvironments (e.g. Roveri et al., 2014; Flecker et al., 2015), continuous continental records in the circum-Mediterranean region have been lacking. Besides being fragmentary, existing European continental records commonly lack the necessary chronological framework to precisely correlate the different phases of the

---

[*] Corresponding author at: Senckenberganlage 25, 60325 Frankfurt, Germany.
E-mail address: maud.meijers@senckenberg.de (M.J.M. Meijers).

https://doi.org/10.1016/j.palaeo.2018.03.001
Received 5 December 2017; Received in revised form 28 February 2018; Accepted 2 March 2018

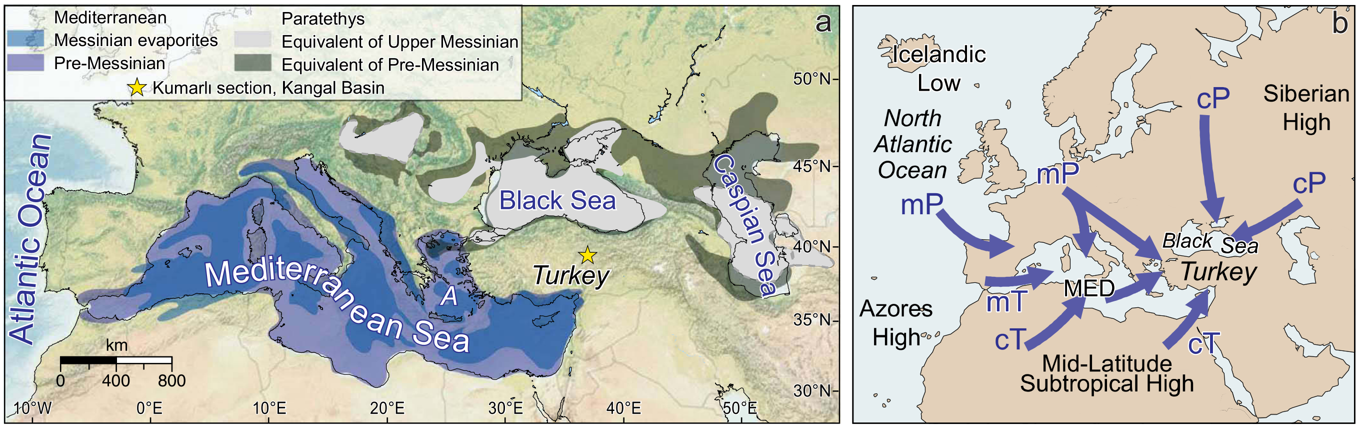

Fig. 1. a) Map of the Mediterranean Sea-Black Sea-Caspian Sea region with outlines of (pre-) Messinian Mediterranean and Paratethys basins and Messinian Mediterranean evaporites (modified from Krijgsman et al., 2010). Yellow star: Kumarlı section, Kangal Basin (this study), A = Aegean.
b) Schematic representation of major air mass trajectories affecting Anatolian climate today including high and low pressure systems (modified from Schemmel et al., 2013): c = continental, m = marine, MED = Mediterranean, P = polar, T = tropical.

MSC with basin development. The MSC occurred entirely within magnetic polarity chron C3r and, in order to resolve the stages of the MSC, one must have additional age information (cyclostratigraphy, stable isotopes, radiometric dating). As a consequence, existing circum-Mediterranean continental records only accurately document paleoenvironmental change prior to, and after the MSC, but lack the necessary precision and resolution across this critical time interval (e.g. Pavlakis, 1999; Fauquette et al., 2006). Atmospheric circulation models that track changes in temperature and precipitation as a result of the (partial) desiccation of the Mediterranean Basin during the MSC predict a large increase in precipitation over North Africa, but no significant change anywhere else around the Mediterranean Sea (Schneck et al., 2010). This pattern is confirmed by Tethys Sea shrinkage models over the period preceding the Messinian (Tortonian, ~11–7 Ma; Zhang et al., 2014). In addition to the environmental effect of the MSC, precession-controlled variations in sediment composition since at least the Serravalian reveal significant longer-period changes in Mediterranean basin-water hydrology (e.g. Rohling et al., 2015). Alternations of marls, limestones, diatomites and sapropels of late Miocene age likely resulted from orbitally driven variations in freshwater input from the African continent as a result of modifications to the African Summer Monsoon (ASM; e.g. Marzocchi et al., 2015). Precessionally driven changes in the ASM modify the composition of the Mediterranean Outflow Waters (MOW) produced in the Mediterranean Sea and delivered to the Atlantic Ocean. Variations in MOW have been shown to affect the Atlantic Meridional Overturning Circulation (AMOC), and consequently northern hemisphere climate during the past 150 kyrs (Bahr et al., 2015). Modeling of MOW modification during the MSC similarly shows its influence on the AMOC (Ivanovic et al., 2014). Given that changes in the thermohaline circulation of the North Atlantic lead to northern hemisphere climate change, one may also expect to find variations in continental N-Mediterranean climate during the MSC.

Here, we provide the first continuous record of paleoenvironmental proxy data (lake carbonate $\delta^{13}C$ and $\delta^{18}O$) through the MSC from the Kangal Basin (Central Anatolia, Turkey), located centrally within the Mediterranean-Paratethys region (Fig. 1a). Based on a combination of magnetostratigraphy, $^{40}Ar/^{39}Ar$ geochronology and existing mammal stratigraphy, we establish a coherent chronology for the upper Miocene to Pliocene fluvio-lacustrine basin infill and evaluate changes in $\delta^{13}C$ and $\delta^{18}O$ with respect to the timing of major sea level change in the basin interior.

The Kangal Basin is located within the semiarid Central Anatolian Plateau (CAP) and river systems currently drain it to three separate marine basins: the Mediterranean Sea, the Black Sea and the Persian Gulf (Fig. 2a). The lake that occupied the Kangal Basin during the Miocene and Pliocene covered an area of at least 150 km × 30 km, therefore integrating climatic conditions over a sizeable portion of the CAP. At present, the CAP interior receives a significant part of its precipitation from the Atlantic Ocean, which is recycled on its way to the CAP over the Mediterranean and Black Sea basins (Fig. 1b; Schemmel et al., 2013). Restricted connectivity of the Mediterranean Sea with the Atlantic Ocean and the Paratethys during the MSC resulted in periods of a negative Mediterranean water balance. This resulted in an increase of δD values in the Mediterranean Basin water by up to 70‰ (Vasiliev et al., 2013, 2015). Eastward transport of moisture evaporating from the Mediterranean and western Paratethys by westerlies may therefore have affected the oxygen isotopic composition of precipitation in central Anatolia. An increase in $\delta^{18}O$ can be expected during the acme of the MSC (5.60–5.55 Ma) when the amount of moisture reaching central Anatolia decreased owing to the drying of the Mediterranean Basin. Conversely, a decrease in $\delta^{18}O$ values can be expected following the MSC owing to an increase in precipitation and a more positive water balance, as observed in other proxy studies (Kayseri-Özer, 2017). In this study, we assess the impact of the Mediterranean environmental crisis on climate and environment in the Eastern Mediterranean continental interior

2. The Messinian (Salinity Crisis) in the Mediterranean and Paratethys basins

The transition into the MSC since the late Tortonian occurred in a stepwise fashion and was driven by long-term orbital forcing with a periodicity of 400 kyr (Kouwenhoven et al., 2003), superimposed on a gradual, tectonically induced Atlantic-Mediterranean gateway closure (e.g. Roveri et al., 2014) that eventually led to the MSC. The MSC has been divided into three stages (e.g. Roveri et al., 2008, 2014): 1) precessionally forced, cyclic gypsum (dominantly selenite)-shale couplet deposition in marginal and deposition of organic-rich shales and dolostones in deeper Mediterranean sub-basins (Primary Lower Gypsum, PLG; 5.971–5.60 Ma); 2) reworking of PLG stage deposits and deposition of evaporites and brecciated limestones in the deep basins (Resedimented Lower Gypsum, RLG; 5.60–5.55 Ma) as a result of widespread subaerial erosion due to a significant drop in sea level. This acme of the MSC coincides with an orbital configuration that resembles that of the onset of the MSC, in which obliquity-controlled glacial stages TG12 and TG14 and their associated environmental impacts (water level and temperature) were likely superimposed (e.g. Van der Laan et al., 2005); and 3) clastic, evaporite-free deposits in the northwestern basins, and precession-driven cyclic alternations that include selenite and cumulate gypsum alongside terrigenous marls and sandstones

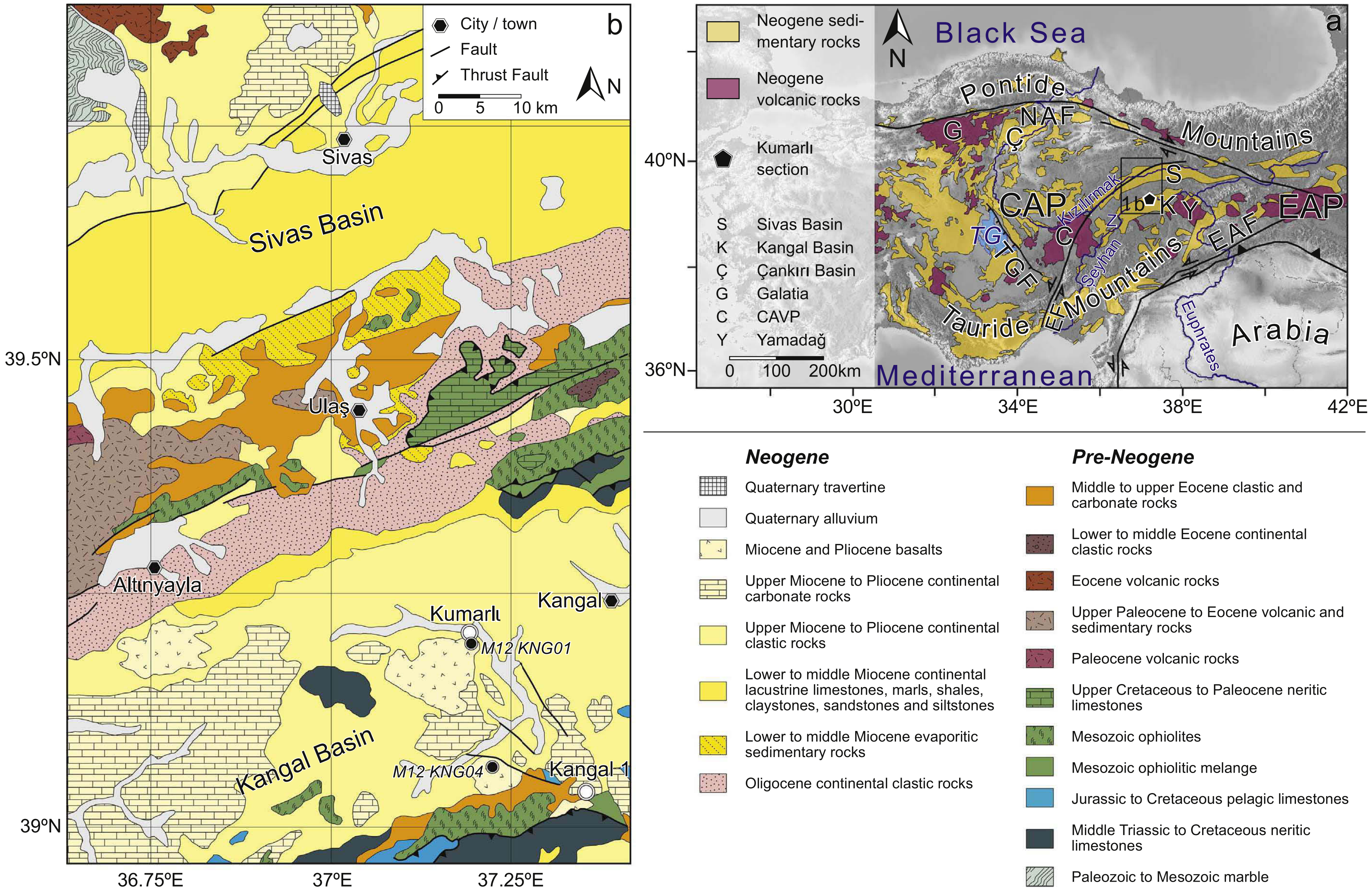

Fig. 2. a) Map of the Central Anatolian (CAP) and East Anatolian (EAP) plateaus within the Arabia-Eurasia collision zone illustrating the widespread occurrence of Neogene volcanics and sedimentary basins. Rectangle indicates map area in b. EAF = East Anatolian Fault, EF = Ecemiş Fault, NAF = North Anatolian Fault, TG = Tuz Gölü, TGF = Tuz Gölü Fault, Z = Zamantı River.

b) Geologic map of the study area (modified from the 1/500.000 scale geological map of Sivas, MTA, General Directorate of Mineral Research and Exploration of Turkey), including locations of the sampled Kumarlı section, as well as the Kangal 1 mammal locality. The basalt that covers the Kumarlı section and was sampled for $^{40}Ar/^{39}Ar$ dating at two locations (M12 KNG01 and M12 KNG04).

(Upper Gypsum, UG; 5.55–5.33) in the southeastern basins. Stage 3 ends at the start of the Zanclean, when connectivity with the Atlantic Ocean was fully restored.

Within the upper part of the Upper Gypsum stage, brackish fauna of Paratethyan affinity are widespread within the Mediterranean Sea; episodic connections of the Mediterranean with the Paratethys via the Aegean Sea occurred since 11 Ma (Popov et al., 2006). Isolation of Paratethys from Mediterranean (and thus Atlantic) waters occurred as a result of a significant base-level drop of the Mediterranean during the MSC, which also led to negative changes in the water budget of the Paratethys (Vasiliev et al., 2013, 2015, 2017).

3. Geology of Anatolia and the study area

The geology and topography of Turkey have been shaped by convergence between the African and Eurasian continents (Şengör and Yilmaz, 1981). During the Late Cretaceous to Paleocene, closure of the Neotethys ocean led to Africa-Eurasia collision in present-day Anatolia (Kaymakci et al., 2009; Meijers et al., 2010). Several large volcanic centers, including the Miocene Yamadağ, Galatia and Central Anatolian volcanic provinces (CAVP; Fig. 2a), formed since the middle Miocene (e.g. Wilson et al., 1997; Gürsoy et al., 2011; Aydar et al., 2012).

Deformation driven by ongoing Africa-Eurasia collision and extension in the Aegean (Fig. 1a) is currently accommodated by the westward escape of the Anatolian microplate between two conjugate strike-slip faults: the North and East Anatolian Faults (NAF and EAF, respectively; Fig. 2a). Following widespread distributed deformation related to the assembly of Anatolia, including significant displacement on the sinistral Ecemiş Fault of the Central Anatolian Fault Zone in the early Cenozoic (Fig. 2a; Koçyiğit and Beyhan, 1998; Jaffey and Robertson, 2001; Umhoefer et al., 2007), a transition from “proto-escape” to “full-escape tectonics” in Anatolia occurred after the middle Miocene, when individual strands of the NAF and EAF started to become active (e.g. Şengör et al., 1985). Since the latest Miocene, central Anatolia has been in a (trans)tensional state (e.g. Özsayin et al., 2014). At present, large parts of central Anatolia are covered by Neogene sedimentary and volcanic rocks (Fig. 2a).

The ENE-WSW oriented Kangal Basin overlies a basement of Paleozoic to Mesozoic sedimentary and volcanic rocks, as well as ophiolites (Fig. 2b). Continental deposition has been prevalent over central Anatolia since the Oligocene, although a number of marine incursions have been identified. The youngest dated marine deposits in the nearby Sivas Basin and its surroundings are of Langhian age (15.97 to 13.82 Ma; Poisson et al., 2016), whereas an extrapolated, younger 9.90 Ma age for the marine deposits was estimated based on a constant sedimentation rate of mid-Burdigalian marine sedimentary rocks (~18.92–17.97 Ma; Ocakoğlu et al., 2018). The youngest lacustrine, flat-lying sedimentary rocks of the Kangal Basin unconformably lap onto middle Miocene sedimentary rocks and consist of claystones, limestones and marls with occasional occurrences of conglomerate. The fluvio-lacustrine successions of the Kangal Basin are capped by a mesa-forming basalt dated at 5.88 ± 0.77 Ma (K-Ar, whole rock age; Platzman et al., 1998). No rocks are exposed above the basalt level. A mammal locality (Kangal 1; Ünay et al., 2003; The NOW Community, 2017) within a laterally equivalent section places the sampled section into MN13 (7.4/6.8–5.3 Ma; Hilgen et al., 2012).

4. (Paleo)environment of central Anatolia

Present-day climatic conditions in the CAP interior are controlled by its position within the Eastern Mediterranean realm, its elevation (> 1 km), as well as its location between two orographic barriers: the Pontide Mountains (Mts) to the north and the Tauride Mts to the south (Schemmel et al., 2013). Mean annual temperature (MAT) in the plateau interior averages 4–10 °C, while mean annual precipitation (MAP) averages 300–500 mm. Surface uplift of the CAP and the development of the orographic barriers since ca. 8 Ma (e.g. Yıldırım et al., 2011; Cosentino et al., 2012), in combination with overall Cenozoic global cooling (Zachos et al., 2001), likely affected the climate and environment of central Anatolia.

During the early and middle Miocene, central Anatolia was characterized by a humid, subtropical climate, with palynoflora-based MAT estimates between 16 °C and 21 °C (Akgün et al., 2007). Estimated MATs dropped to ~14–17 °C by the early late Miocene. MAP estimates for the early to early late Miocene based on palynofloras range between 1000 mm and 1400 mm (Akkiraz et al., 2011); estimates for the northern CAP are slightly lower at ~900 mm (Mazzini et al., 2013). Temperature reconstructions based on a review of floral data in Anatolia show an increase in temperature from the Tortonian to the beginning of the Messinian, followed by a significant temperature drop throughout the Messinian (Kayseri-Özer, 2017). MAPs average ~1200 mm during the late middle Miocene and late Miocene, with the exception of estimated MAPs of < 1000 mm during the earliest Messinian. Plant-derived MAP estimates increase distinctly across the Mio-Pliocene boundary (Kayseri-Özer, 2017).

Phytolith data from central Anatolia indicate the presence of open-habitat grassland alongside woodland and forest vegetation throughout the Miocene (Strömberg et al., 2007). Open-habitat grassland becomes increasingly dominant during the late Miocene (Strömberg et al., 2007), which is in agreement with observations from mammal studies in the nearby Sivas Basin (Fig. 2; e.g. Kaya and Kaymakçı, 2013). Similarly, a recent study based on mammal dental ecometrics and faunal similarity shows that mammal faunas from the late Miocene of central Anatolia adapted to increasingly open habitats as a part of the intercontinentally developing Old World savannah paleobiome (Kaya et al., 2018). Based on sciurid fossils, a late Miocene central Anatolian paleoenvironment composed of forested areas with tree and flying squirrels, as well as an open environment with ground squirrels was reconstructed (Bosma et al., 2013). The study includes two species of ground squirrels that were retrieved from the Kangal 1 mammal site. Paleovegetation reconstructions based on Messinian micro- and macrofauna show a large variety of vegetation types over central Anatolia, including mixed mesophytic forests, broad-leaved evergreen forests and xeric open woodlands or steppes, including areas with high percentages of zonal herb components (Kayseri-Özer, 2017). During the Pliocene, the values of the sclerophyllous, legume-like and zonal herb components increased over Anatolia. A relative increase of broad-leaved components in central Anatolia with respect to western Anatolia may result from a higher topography over central Anatolia in the Pliocene (Kayseri-Özer, 2017).

In contrast to today, vast parts of Anatolia were covered with lakes during the late Miocene, and some regions have intermittently hosted extensive lakes well into the Holocene, such as the area west of the Tuz Gölü Fault (Fig. 2a; e.g. Leng et al., 1999; Jones et al., 2007; Dean et al., 2013). The only sizeable present-day lake is the highly evaporative Tuz Gölü (i.e. salt lake). The lake that once covered the Kangal Basin may have been well over 150 km long and about 30 km wide. Its size suggests that this lake was fed by a large river system, therefore integrating climatic and environmental conditions over a significant part of Anatolia. Moisture that reached the Kangal region from the Atlantic, Black Sea and Mediterranean basins likely had to cross the orographic barriers of the Pontide and Tauride Mts (Yıldırım et al., 2011; Schemmel et al., 2013). Lake Kangal may, therefore, have recorded changes in moisture sources and fluxes during the MSC. Interestingly, the watershed between the Mediterranean Sea (Seyhan River) and the Persian Gulf (Euphrates River) is currently situated in the Kangal Basin (Fig. 2a). The topographic ridge that forms the northern margin of the Kangal Basin separates the basin from the catchment area of the Kızılırmak River, which flows towards the Black Sea.

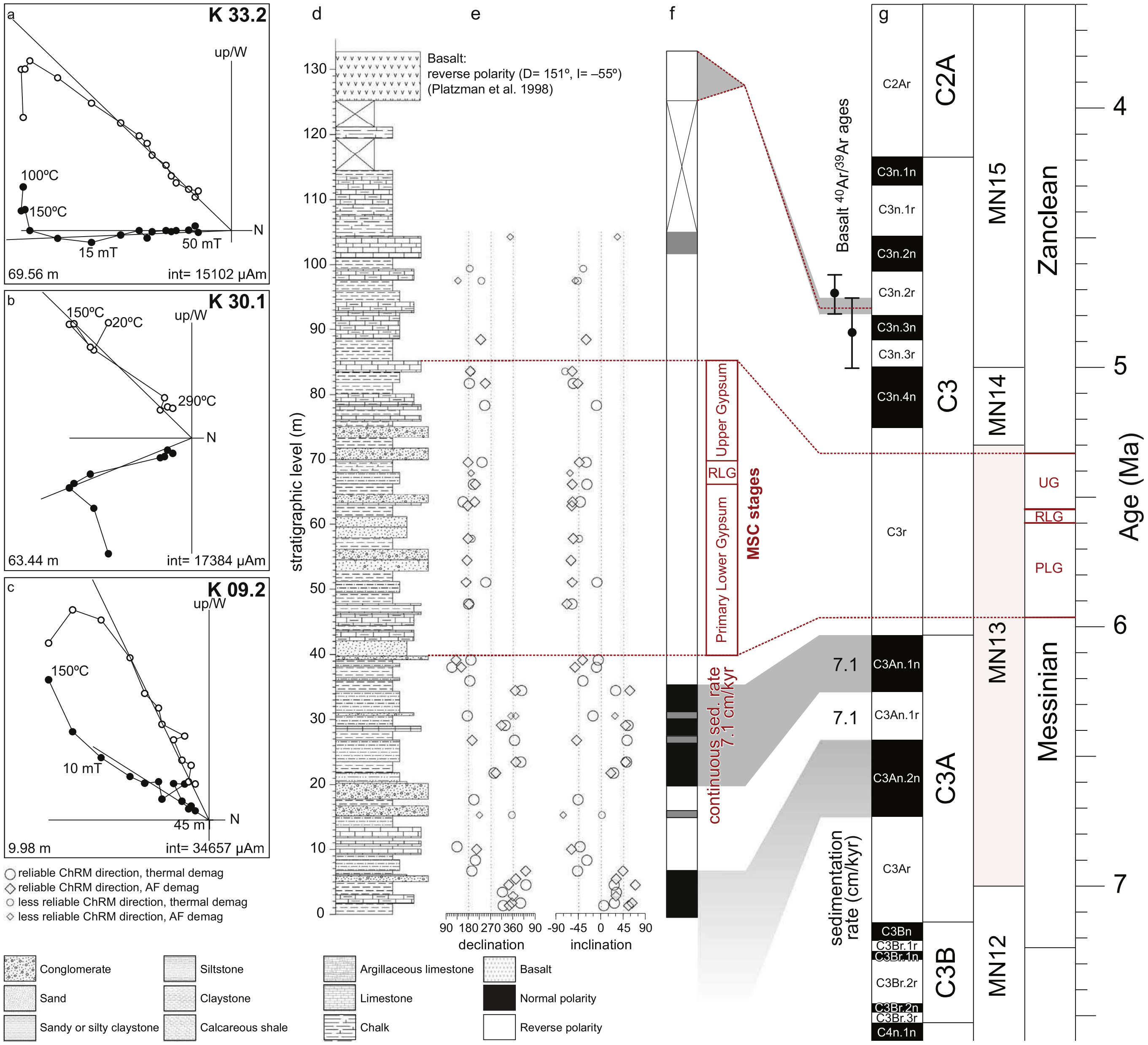

Fig. 3. a–c) Examples of representative orthogonal vector diagrams (Zijderveld, 1967). Closed (open) circles indicate projection on the horizontal (vertical) plane; int = intensity of the lowest displayed demagnetization step. Stratigraphic level of each diagram indicated in the lower left corner.

d) Stratigraphic log of the sampled Kumarlı section.

e) Paleomagnetic results (declination, inclination of the ChRM). For symbols we refer to the legend in the figure.

f) (Magneto)stratigraphy of the Kumarlı section (black = normal, white = reverse) and its correlation to the GPTS (g), including the associated sedimentation rates. Grey-colored intervals indicate mixed polarity levels or single levels with an opposing polarity compared to the surrounding levels. The three MSC stages (PLG, RLG, UG), as well as the age of the basalt are correlated to the stratigraphy using a continuous sedimentation rate of 7.1 cm/kyr after chron C3An.1n.

g) Time scale for the late Miocene (Tortonian, Messinian) and early Pliocene (Zanclean), including the Mammal Neogene (MN) Units as Interval Biochrons, as well as the chronostratigraphy (black: normal polarity, white: reverse polarity; Hilgen et al., 2012). The mammal locality (Kangal 1; Ünay et al., 2003; The NOW Community, 2017) within a laterally equivalent section places the sampled section into MN13 (7.4/6.8–5.3 Ma).

PLG: Primary Lower Gypsum, RLG: Resedimented Lower Gypsum (MSC acme) and UG: Upper Gypsum.

5. Methods

5.1. Field approach and sampling

The Kumarlı section was sampled for paleomagnetism and carbon ($\delta^{13}C$) and oxygen ($\delta^{18}O$) isotope geochemistry within the continental upper Miocene Kangal Basin (Fig. 2). The logged section covers 135 m (Fig. 3d); it consists of an alternation of (carbonaceous) claystones, (clayey) limestones, chalk, and marls. A few conglomerate beds occur throughout the section. Some of the conglomerate beds are cross-bedded and/or contain clasts that likely eroded from nearby Mesozoic ophiolites and ophiolitic melanges (Fig. 2b).

The Kumarlı section was first sampled for paleomagnetic analyses (total number of demagnetized cores: 78) in 2011, when 45 levels were sampled within the first 104 m of the logged stratigraphy. At each level, two to three paleomagnetic cores (2.54 cm diameter) were sampled using a gasoline-powered motor drill or a generator-powered electric drill. The cores within each level were numbered according to their stratigraphic order, i.e. core 1.1 was taken from a level older than (or equal to) core 1.2. Paleomagnetic cores were oriented using a magnetic

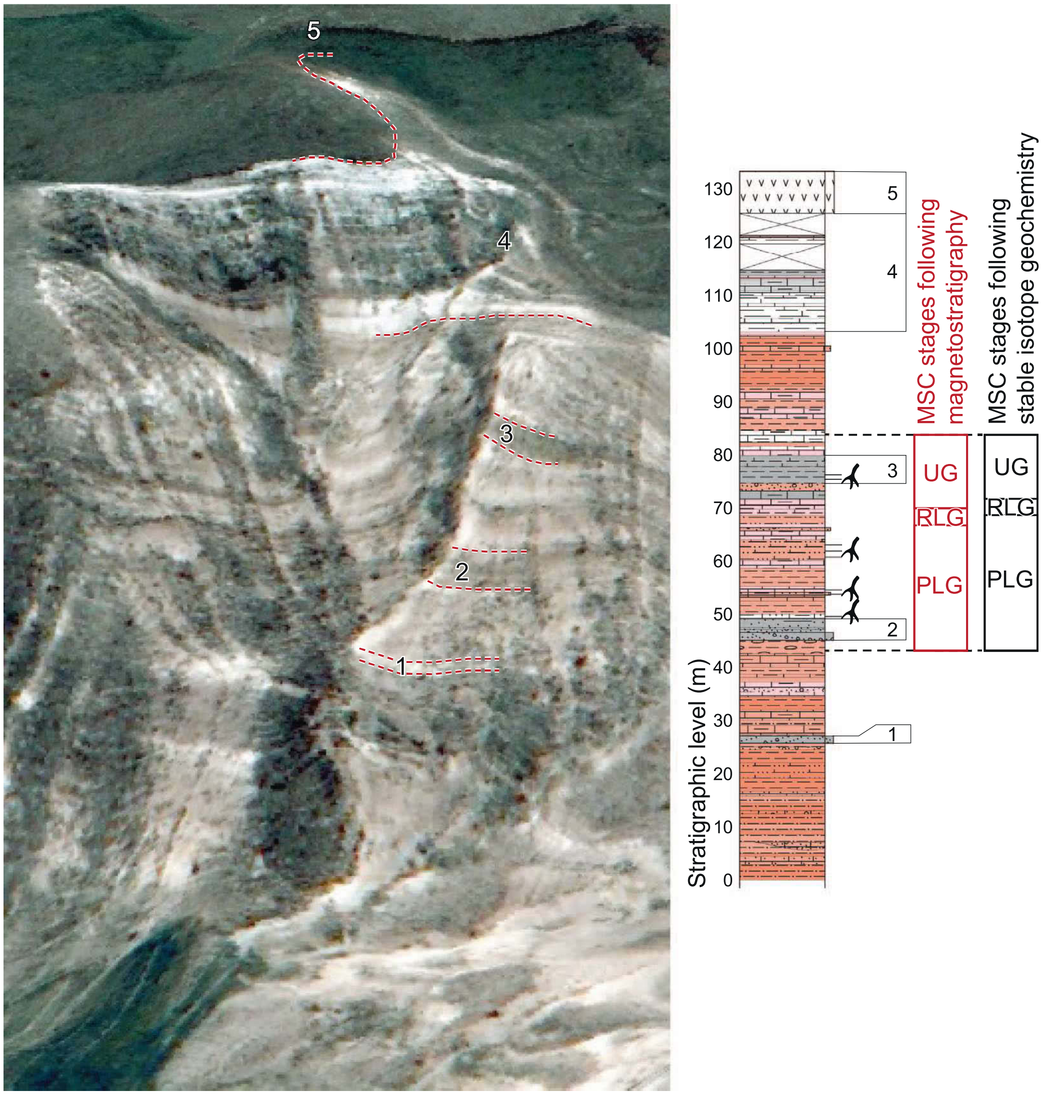

Fig. 4. Satellite imagery (DigitalGlobe Inc.; provided through the Polar Geospatial Center, University of Minnesota, C. Lefebvre) of the Kumarlı section and its correlation to the stratigraphic log (Figs. 3 and 9), as well as to the MSC stages. PLG: Primary Lower Gypsum, RLG: Resedimented Lower Gypsum (MSC acme) and UG: Upper Gypsum.

compass. Magnetic declinations were corrected for ~5.2° magnetic declination. Samples were cut into standard paleomagnetic specimens (2.2 cm height) in the laboratory.

Samples for stable isotope analyses were collected in 2014, and the Kumarlı section was newly logged. A correlation of the sedimentary log to a satellite image of the section is provided in Fig. 4. The stratigraphic log of the previous field season along with the GPS localities of the paleomagnetic sampling levels enabled us to find the paleomagnetic coring holes preserved in the more competent levels and correlate the newly logged section to the section sampled for paleomagnetism. Overall, 101 levels were sampled for stable isotope analysis throughout the entire section (i.e. up to 125 m).

Two samples were taken for $^{40}Ar/^{39}Ar$ dating from the basalt that caps the section; they provide a minimum age for the section. One sample was taken at the top of the section (M12 KNG01), and the other one was taken ~15 km south of the section from what is, based on its position, most likely the same basalt (M12 KNG04, Fig. 2b).

5.2. $^{40}Ar/^{39}Ar$ geochronology

The $^{40}Ar/^{39}Ar$ analyses of the two whole-rock basalt samples (M12 KNG01 (871–02) and M12 KNG04 (859-02); Fig. 2b) were performed at the U.S. Geological Survey (USGS) in Denver (USA). The crushed whole-rock samples were irradiated with standards in 3 separate irradiations for 0.5, 3, and 5 MWh, respectively, in the central thimble position of the USGS TRIGA reactor (Dalrymple et al., 1981), while being rotated at 1 rpm. Following irradiation, the samples and standards were loaded to a stainless steel sample holder with tweezers and then placed into a laser chamber with an externally pumped ZnSe window. The incremental heating data that are reported represent results from individual mineral grains and/or rock fragments. The volume of the mostly stainless steel vacuum extraction line, including a cryogenic trap operated at −130 °C and two SAES™ GP50 getters (one operated at room temperature, one at 2.2A), is estimated at ~450 cm^3. A combination of turbo molecular pumps and ion pumps maintains steady pressures of $< 1.33 \times 10^{-7}$ Pa within the extraction line. Samples were incrementally heated in steps of 90 s, by controlled power output of a 50 W CO_2 laser equipped with a beam-homogenizing lens, which results in a uniform energy distribution over the entire sample surface. Any sample gas that was released during laser heating was exposed to the cryogenic trap and was further purified for an additional 120 s by exposure to both the cryogenic trap and the SAES getters. The sample gas was expanded into a Thermo Scientific ARGUS VI™ mass spectrometer and argon isotopes were analyzed simultaneously using four faraday detectors (^{40}Ar, ^{39}Ar, ^{38}Ar, ^{37}Ar) and one ion counter (^{36}Ar). Detector calibration was carried out using a fixed reference voltage on the

faraday detectors. The ion counter was calibrated relative to the faraday detectors by regular air pipette measurements, and the detector discrimination was monitored by the $^{40}Ar/^{39}Ar$ ratios of Fish Canyon sanidine measurements. Following 10 min of data acquisition, time zero intercepts were fit to the data (using parabolic and/or linear best fits) and corrected for backgrounds, detector inter-calibrations, and nucleogenic interferences. The Mass Spec computer program (A. Deino, Berkeley Geochronology Center) was used for data acquisition, age calculations, and plotting. All $^{40}Ar/^{39}Ar$ ages reported in Supplementary Table S1 and Fig. 5 are referenced to an age of 28.201 ± 0.046 Ma for Fish Canyon sanidine (Kuiper et al., 2008), the decay constants of Min et al. (2000), and an atmospheric $^{40}Ar/^{36}Ar$ ratio of 298.56 ± 0.31 (Lee et al., 2006). Laser fusion of more than 10 individual Fish Canyon Tuff sanidine crystals at each closely monitored position within the irradiation package resulted in neutron flux ratios reproducible to $\leq 0.25\%$ (2σ). Isotopic production ratios were determined from irradiated CaF_2 and KCl salts. For this study the following values were measured: $(^{36}Ar/^{37}Ar)_{Ca} = (2.4 \pm 0.05) \times 10^{-4}$; $(^{39}Ar/^{37}Ar)_{Ca} = (6.59 \pm 0.10) \times 10^{-4}$;
and $(^{38}Ar/^{39}Ar)_K = (1.29 \pm 0.03) \times 10^{-2}$. Cadmium shielding during irradiation prevented any measurable $(^{40}Ar/^{39}Ar)_K$. For the calculation of the plateau ages we required three or more consecutive heating steps that released $\geq 50\%$ of the total ^{39}Ar and also had statistically (2σ) indistinguishable $^{40}Ar/^{39}Ar$ ages.

5.3. Paleomagnetism and rock magnetism

Paleomagnetic specimens were either demagnetized using stepwise thermal demagnetization or by a combination of stepwise thermal and alternating field (AF) demagnetization techniques (Fig. 3a–c) at the paleomagnetic laboratory Fort Hoofddijk, Department of Earth Sciences, Utrecht University (Netherlands). When a combination of thermal and AF demagnetization was applied, specimens were (stepwise) demagnetized up to 150 °C prior to AF demagnetization to remove possible stress in magnetite grains caused by surface oxidation at low temperatures (Van Velzen and Zijderveld, 1995). Specimens from a number of levels were demagnetized using thermal and combined thermal and AF demagnetization to compare the reproducibility of both techniques.

The demagnetization of the natural remanent magnetization (NRM) is displayed in orthogonal vector diagrams (Zijderveld, 1967). Specimen characteristic remanent magnetization (ChRM) directions were determined using principal component analysis (Kirschvink, 1980) on approximately five to eight successive demagnetization steps (Supplementary Table S2).

Site means, as well as virtual geomagnetic poles (VGPs) and their means, were calculated from the individual ChRM directions (Fig. 6). A fixed 45° cutoff was applied to the VGP distribution and site-mean statistics were calculated using Fisher (1953). The error in declination (ΔD_x) and inclination (ΔI_x) were determined following Butler (1992). We perform a reversal test following the coordinate bootstrap test of Tauxe (2010), using the platform-independent web portal Paleomagnetism.org (Koymans et al., 2016; Fig. 7). The same portal is used to assess paleosecular variation, following the N-dependent criteria of Deenen et al. (2011, 2014).

Magnetic susceptibility as a function of temperature (K/T curves; Fig. 8) was measured using an MFK1-FA Susceptibility Bridge with CS4 Furnace (Agico; 200 Am^{-1} and 976 Hz) at the Institute for Rock Magnetism in the N.H. Winchell School of Earth Sciences, University of Minnesota, Minneapolis (USA). Approximately 0.30–0.45 g of powdered rock was heated to successively higher temperatures (max. 700 °C) in air to monitor possible chemical alteration of the magnetic minerals.

5.4. Stable isotope geochemistry

Stable isotope analysis was carried out at the joint Goethe University—Senckenberg BiK-F Stable Isotope Facility in Frankfurt (Germany). Whole-rock sample powders were digested in orthophosphoric acid and analyzed as CO_2 in continuous flow mode using a Thermo MAT 253 mass spectrometer interfaced with a Thermo GasBench II. Analytical procedures are according to Spötl and Vennemann (2003). Raw isotopic ratios were calibrated against a Carrara marble in-house standard and against NBS18 and NBS19 carbonate reference materials. Final isotopic ratios are reported against Vienna Standard Mean Ocean Water (V-SMOW) for $\delta^{18}O$ and Vienna Pee Dee Belemnite (V-PDB) for $\delta^{13}C$ (Fig. 9). Analytical uncertainties are typically better than 0.10‰ ($\delta^{18}O$) and 0.07‰ ($\delta^{13}C$). The carbonate content of each sample was derived from standard-sample total peak area ratios. The reported carbonate contents are precise to within 10%. $\delta^{13}C$ and $\delta^{18}O$ values from a total of 101 samples are provided in the supporting information. We looked at $\delta^{18}O$-$\delta^{13}C$ covariance using a total least squares (TLS) regression analysis combined with a novel approach to bootstrapping (Pastor-Galán et al., 2017), a method in which observational errors or uncertainties in both dependent and independent variables are taken into account. The method provides bootstrapped confidence limits and a test of linearity; it has been implemented as an orocline test in Paleomagnetism.org but can be used on nearly all types of data.

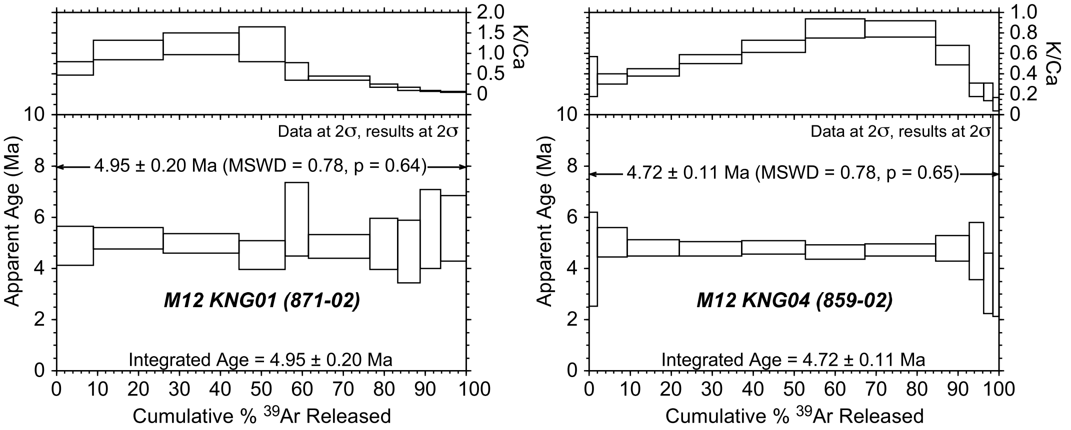

Fig. 5. $^{40}Ar/^{39}Ar$ CO_2-laser incremental-heating data of samples M12 KNG01 and M12 KNG04 from the basalt at the top of the Kumarlı section. MSWD: mean square of weighted deviates. K/Ca ratios plotted for reference.

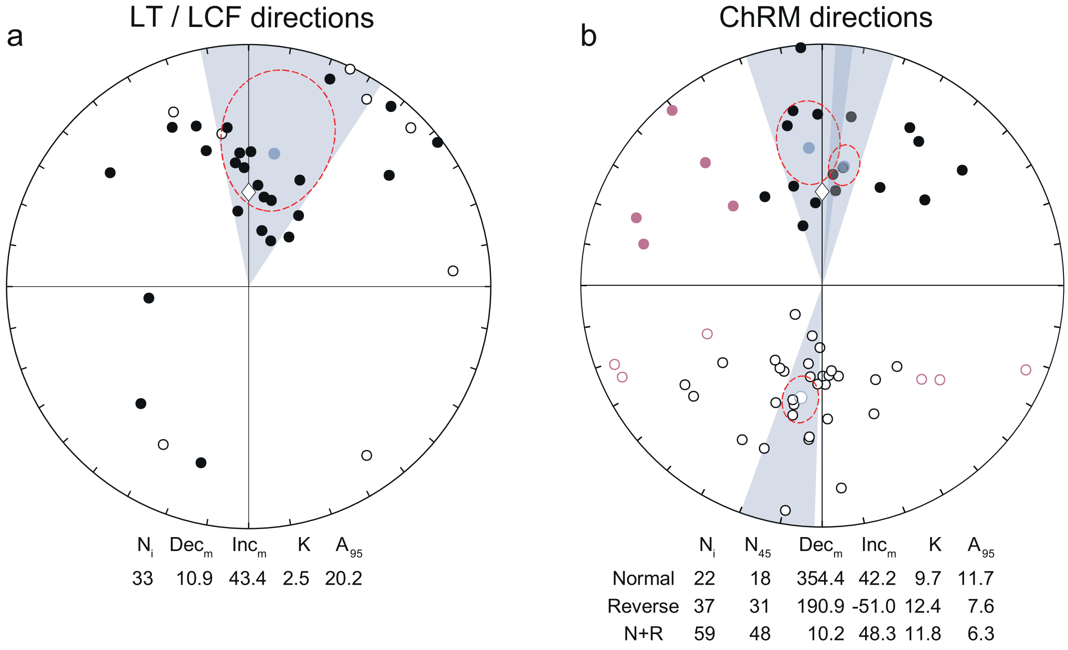

N_i	Dec_m	Inc_m	K	A_{95}
33	10.9	43.4	2.5	20.2

	N_i	N_{45}	Dec_m	Inc_m	K	A_{95}
Normal	22	18	354.4	42.2	9.7	11.7
Reverse	37	31	190.9	-51.0	12.4	7.6
N+R	59	48	10.2	48.3	11.8	6.3

Fig. 6. a–b) Equal area projections of the LT/LC (a) and ChRM (b) directions. Open (closed) symbols denote projection on the upper (lower) hemisphere. The mean ChRM directions (N + R) were calculated after applying a 45° fixed cutoff to the respective VGP distributions of the normal and reverse polarity data sets; pink symbols indicate directions that were removed by the cutoff; white diamonds indicate the geocentric axial dipole (GAD) direction at the sampling site. Blue symbols indicate the mean LT/LC and ChRM directions and their error envelope (red dotted line) and ΔD_x (shaded blue area). N_i = number of interpreted directions, N_{45} = number of directions after the application of the 45° fixed cutoff, Dec_m (Inc_m) = mean declination (inclination) of the LT/LCF or ChRM directions with the dispersion parameter (K) and cone of confidence (A_{95}) of the corresponding VGP distribution.

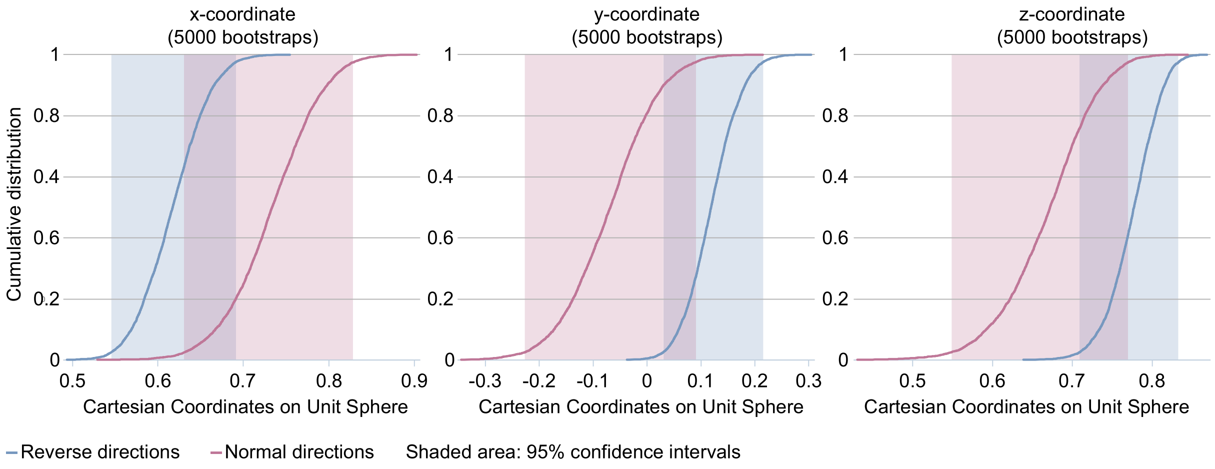

Fig. 7. Cumulative distributions of Cartesian coordinates of means of pseudo-samples drawn from the normal and reverse polarity data (Fig. 6b). The shaded confidence intervals contain 95% of each set of components. The confidence bounds of the normal and reverse polarity data sets overlap in all three components (x, y, z) and therefore pass the bootstrap reversal test (Tauxe, 2010).

6. Results

6.1. $^{40}Ar/^{39}Ar$ geochronology

For both analyzed basalt samples, the plateau age and integrated age are identical; the requirements for the calculation of a plateau age apply to all heating steps (Fig. 5). The plateau ages for M12 KNG01 (871-02) and M12 KNG04 (859-02) are 4.95 ± 0.20 Ma and 4.72 ± 0.11 Ma, respectively, and are thus indistinguishable within their uncertainties. The new ^{40}Ar/^{39}Ar ages are younger than a previously determined whole-rock K-Ar age determination of 5.88 ± 0.77 Ma for this basalt (Platzman et al., 1998), although our oldest age (4.95 ± 0.20 Ma) is, within error, statistically indistinguishable from the K-Ar age. Many of the samples on which K-Ar dating was performed contain a high fraction of non-radiogenic argon (Platzman et al., 1998), which may be the cause for the discrepancy between the K-Ar and ^{40}Ar/^{39}Ar ages.

The new ^{40}Ar/^{39}Ar ages are also slightly younger than the MN13 mammal age (7.4/6.8–5.3 Ma; Ünay et al., 2003; The NOW Community, 2017) that was reported for the sedimentary rocks that underlie the basalt.

6.2. Paleomagnetic and rock magnetic results

Susceptibility as a function of temperature (K/T) of some samples gradually increases up to ~300 °C (Fig. 8). This maximum can be interpreted as a Hopkinson peak, which marks the transition from blocking temperatures to Curie temperatures for magnetic minerals (Hopkinson, 1989) followed by a sharp susceptibility drop associated with the Curie temperature (T_c). The susceptibility reaches a minimum

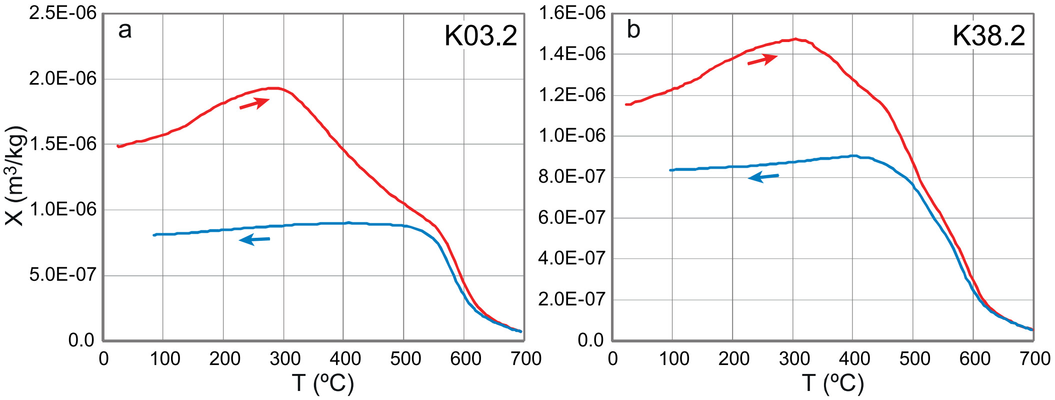

Fig. 8. Representative examples of the susceptibility (K) versus temperature measurements (performed in air). Red (blue) curve denotes heating (cooling). The gradual increase in K up to ~300 °C (which can be interpreted as a Hopkinson peak) marks the transition from blocking temperatures to Curie temperatures (Hopkinson, 1989). Minimum K is reached > 580 °C, indicating that maghemite is the dominant magnetic carrier. The lower K of the cooling curves indicates oxidation of maghemite to hematite.

well above 580 °C (i.e. the T_c of magnetite), which seems to indicate that maghemite (γFe_2O_3) is the dominant magnetic carrier. The final cooling step is characterized by lower susceptibilities compared to the first heating cycles, indicating that the sample underwent further oxidation, e.g. by conversion of maghemite to hematite, which has a lower spontaneous magnetization.

Upon demagnetization, a low temperature (LT) or low coercive (LC) component was identified between ~25–100 °C and ~150 °C–10 mT in 33 of 78 specimens (Figs. 3a–c, 6a; Supplementary Table S2). Its mean direction (D = 10.9° ± 22.4° *I* = 43.4° ± 26.0°; Table 1) includes the geocentric axial dipole direction for the latitude of the section, and is therefore clearly a present-day field overprint. In 59 of the 78 demagnetized specimens, a high temperature (HT) or high coercive force (HCF) component was identified. We interpret this component as the ChRM. The interval over which the HT/HCF component was determined is rather variable, and it includes demagnetization steps up to 420 °C or 50 mT (Supplementary Table S2). The ChRM directions yield both reverse (N = 37) and normal polarities (N = 22). Thermal and AF demagnetization of the ChRM generally yields similar results (Fig. 3e), except for three levels at approximately 15, 26 and 31 m (levels K12, K16 and K18, respectively). The normal and reverse polarity distributions are identical at the 95% confidence level (Fig. 7) using the coordinate bootstrap test of Tauxe (2010); this signifies a positive reversal test. Combining the normal and reverse directions and applying a 45° fixed cutoff on the combined VGP distribution, leads to a mean ChRM direction of D = 10.3° ± 7.2°, *I* = 48.3° ± 7.3° (N = 48; Table 1). If we compare this direction to the expected direction from the apparent polar wander path (of Torsvik et al., 2012) calculated for Eurasia, it appears that the calculated direction falls just within error on the pole path. The expected declination is (hardly significantly) clockwise with respect to North but falls within the expected declination for Eurasia (2.6° ± 2.5°) at this position and age (~6 Ma). Although the inclination is shallower than expected from the pole path (~57° ± 2°), it falls within the respective error margins. The lower inclination is likely caused by inclination shallowing, which is a (post-)depositional process that may lead to an underestimation of paleolatitude in sedimentary rocks.

6.3. Magnetic polarity pattern

The Kumarlı section starts with a first normal polarity interval up to 6.6 m, which is followed by a first reverse polarity interval of 13.1 m (from 6.6–19.7 m; Fig. 3e,f). This first reverse polarity interval includes one less reliable transitional specimen at 15.2 m. The second normal polarity interval spans 15.5 m (from 19.7–35.2 m). This normal polarity interval includes two levels each with a single reverse polarity specimen, at 26.8 m and at 30.5 m, but both levels also include normal polarity specimens. The second reverse polarity interval is long and spans 64.2 m (between 35.2 m and 99.4 m). Above this level, we interpreted one specimen as yielding a normal polarity (104.2 m), which could possibly represent the start of the next normal polarity chron (C3n.4n). The demagnetization diagram of the specimen is rather erratic, however. The study by Platzman et al. (1998) reveals that the basalt that covers the section (125.0 m and up) has a reverse polarity (D = 151°, *I* = −55°, N = 5 from a single basalt flow).

6.4. Stable isotope geochemistry

The $\delta^{13}C$ and $\delta^{18}O$ results (n = 101) from the Kumarlı section yield mean values of $\delta^{13}C = -7.6 \pm 0.9‰$ (1σ) and $\delta^{18}O = 23.0 \pm 1.1‰$ (Fig. 9, Supplementary Table S3). As indicated by the low standard deviations of the $\delta^{13}C$ and $\delta^{18}O$ values, no large overall trends in $\delta^{13}C$ and $\delta^{18}O$ can be observed throughout the section: $\delta^{13}C$ values range between −9.5 and −4.8‰, whereas $\delta^{18}O$ values range between 20.4 and 25.1‰. Throughout the section, we observe a positive linear correlation (i.e. covariance) between $\delta^{13}C$ and $\delta^{18}O$, with a Pearson's coefficient of 0.713 (Supplementary Fig. S1).

Based on variations and variability in $\delta^{13}C$ and $\delta^{18}O$, we identify the following five intervals:

1) 0–42 m (KU1-KU39), with $\delta^{13}C = -7.4 \pm 0.8‰$ and $\delta^{18}O = 23.0 \pm 1.1‰$;
2) 42–64 m (KU40-KU54), with $\delta^{13}C = -7.5 \pm 0.5‰$ and $\delta^{18}O = 22.9 \pm 0.7‰$, which is characterized by mean $\delta^{13}C$ and $\delta^{18}O$ values that are near-identical to those in interval 1, but with lower standard deviations;
3) 64–83 m (KU55-KU71), with $\delta^{13}C = -7.2 \pm 0.6‰$ and $\delta^{18}O = 23.2 \pm 1.0‰$, which includes a number of episodes with higher $\delta^{13}C$ (> −6‰) and $\delta^{18}O$ (> 24‰) values;
4) 84–106 m (KU72-KU91), with $\delta^{13}C = -8.4 \pm 0.6‰$ and $\delta^{18}O = 22.3 \pm 1.0‰$, which is characterized by a drop in $\delta^{13}C$ and $\delta^{18}O$ of ~1‰ at 84 m compared to intervals 1–3;
5) 106–121 m (KU92-KU101), with $\delta^{13}C = -7.3 \pm 0.6‰$ and $\delta^{18}O = 24.3 \pm 1.2‰$ attaining values similar to intervals 1–3.

7. Discussion

7.1. Magnetic carriers, rotations and paleolatitudes

The paleomagnetic and rock magnetic results (K/T measurements) lead us to conclude that the magnetic carrier of the ChRM in the Kumarlı section is (cation-deficient) magnetite or maghemite (Figs. 3a–c, 8). We observed a rather large variation in the demagnetization steps that were included in the calculation of the ChRM. This

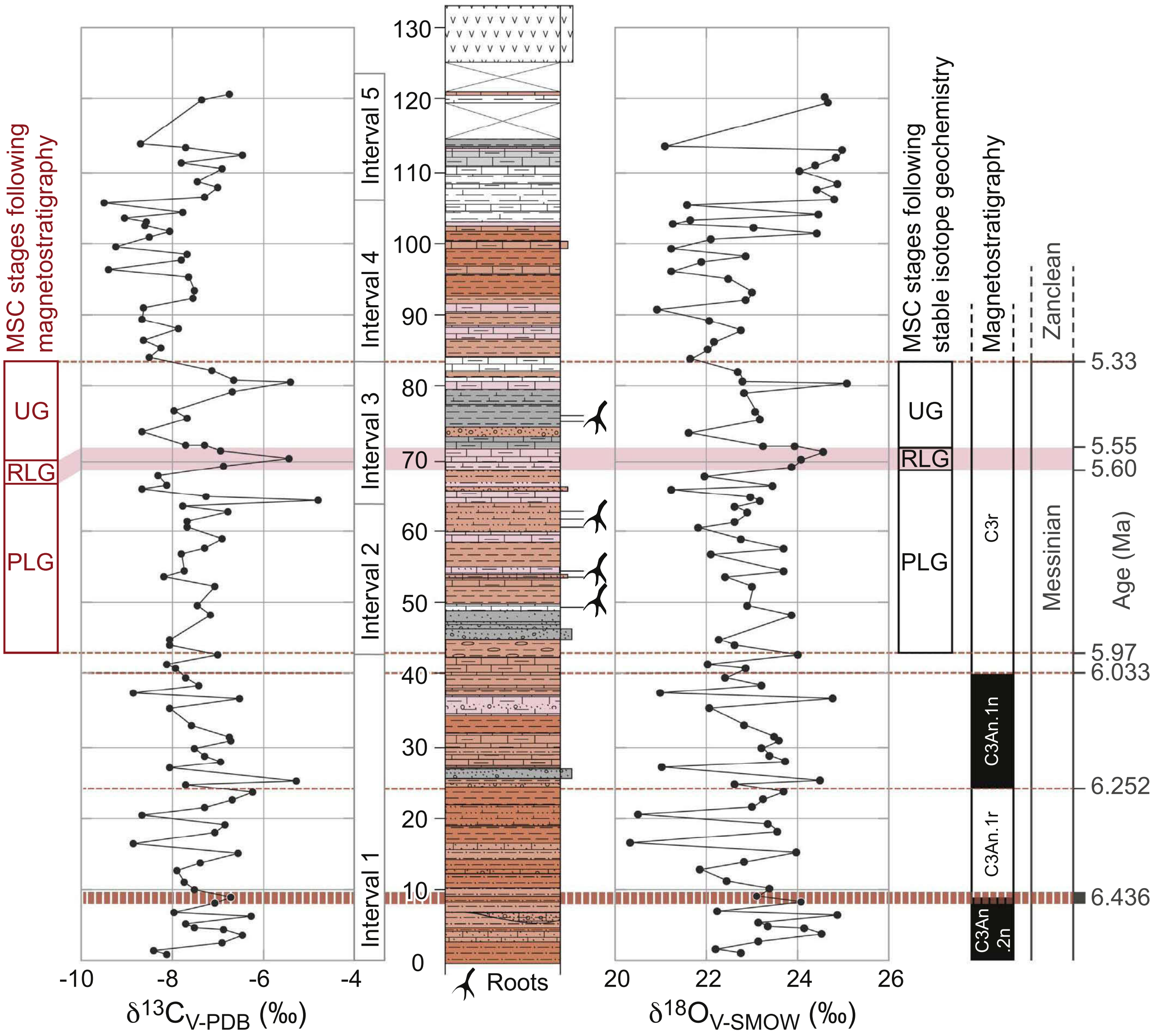

Fig. 9. Stratigraphy, $\delta^{18}O$ and $\delta^{13}C$ values for the Kumarlı section. The intervals and stages of the Messinian Salinity Crisis according to the magnetostratigraphy are indicated (in red), as well as the most likely correlations following the stable isotope results (in black). Additionally, the two rightmost panels indicate the levels of the magnetic polarity reversals and their corresponding polarity chrons and ages. The boundary between chron C3An.2n and C3An.1r is approximate and represented by a thick, dashed line. Legend for the stratigraphic log as in Fig. 3. Intervals 1–5 are discussed in the text.

variation may be caused by the large variety of rock types, resulting in a wide range of magnetic minerals, as well as variable magnetic grain sizes and degrees of oxidation.

The combined normal and reverse ChRM directions of the sedimentary rocks of the Kangal section are rotated slightly clockwise (D = 10.3°, ΔD_x = 7.2°) with respect to the geographic North, but there is no significant rotation with respect to the direction expected from the APWP (of Eurasia) at this age and locality. Published paleomagnetic results from upper Miocene and younger rocks from the study region (Sivas and Kangal basins; Gürsoy et al., 1997; Platzman et al., 1998) were all sampled in basaltic rocks. Given the low number of individual basalt flows that were sampled at each locality (N_{flows} = 1 or 2), paleosecular variation cannot sufficiently have been recorded and therefore was unlikely averaged out in the studies by Gürsoy et al. (1997) and Platzman et al. (1998). Collectively, however, they suggest a counterclockwise rotation, which we do not observe in the upper Miocene to Pliocene Kangal Basin deposits.

7.2. Correlation of the Kumarlı section to the Geomagnetic Polarity Time Scale (GPTS)

Stratigraphic ages for the Kumarlı section based on small mammal biochronology are available by direct correlation of lacustrine units with the nearby Kangal 1 locality (~24 km SSE from the sampled section, Fig. 2b; Ünay et al., 2003; The NOW Community, 2017), placing the Kumarlı section at MN13, i.e. 7.4/6.8–5.3 Ma (Hilgen et al., 2012). Kangal 1 is located in a quarry that was mined for lignite deposits that occur at the base of the quarry. We did not encounter lignite deposits in our sampled section indicating that these lignites are either absent at the Kumarlı site or that the Kumarlı section does not reach sufficiently deep into the local stratigraphy. Kangal 1, however, was located closer to the southern paleo-lakeshore (Fig. 2b), which is presently defined by a topographic ridge of deformed pre-Neogene deposits, and therefore likely exhibits differing facies and stratigraphy. In concordance with the new $^{40}Ar/^{39}Ar$ ages, the mammal stratigraphic age places the Kumarlı

Table 1

Summary of the paleomagnetic results. Of the 45 sampled levels, 78 samples (specimens) were demagnetized. N_i = number of interpreted directions, N_{45} = number of directions passing the 45° fixed cutoff; D = declination, I = inclination and their associated uncertainties determined from the A95 (ΔD_x and ΔI_x, respectively), with the corresponding dispersion parameter (k) and cone of confidence (α_{95}) of the directional distribution. A95, K = cone of confidence and dispersion parameter of the virtual geomagnetic pole distribution. To represent paleosecular variation, A95 should be between a minimum ($A95_{min}$) and maximum ($A95_{max}$) value (Deenen et al., 2011). The A95 of the LT/LCF component clearly has a too high value that suggests an additional source of scatter.

KUMARLI	N_i	N_{45}	**D**	ΔD_x	**I**	ΔI_x	**k**	a_{95}	**K**	$A95_{min} < \mathbf{A95} < A95_{max}$
Low T/CF	33	– –	10.9	22.4	43.4	26.0	2.5	20.6	2.5	3.0 < 20.2 < 9.1
High T/CF - normal	22	18	354.4	12.9	42.2	15.5	9.5	11.8	9.7	3.8 < 11.7 < 13.3
High T/CF - reverse	37	31	190.9	9.0	−51.0	8.4	14.5	7.0	12.4	3.0 < 7.6 < 9.4
High T/CF - all normal	59	48	10.2	7.2	48.3	7.3	13.0	5.9	11.8	2.6 < 6.3 < 7.3

Section Base (K1): 39.20495° N, 37.19937° E.

section in the latest Miocene(−earliest Pliocene).

Based on our magnetic polarity pattern and the $^{40}Ar/^{39}Ar$ ages, we correlate the first normal polarity interval at the base of the section to chron C3An.2n of the GPTS (Hilgen et al., 2012), and the second normal polarity interval of the section to chron C3An.1n, resulting in sedimentation rates of 7.1 cm/kyr for C3An.2n and C3An.1r (Fig. 3f,g). The long reverse polarity interval that starts at 35.2 m can be correlated to chron C3r. One of the single reliable reverse polarity specimens at 26.8 m and at 30.5 m may correspond to the cryptochron that has been reported in a Moroccan and a Spanish section (Sierro et al., 2001; Krijgsman et al., 2004), although we must note that reliable normal polarities were recorded at the same levels within our section (Fig. 3e). Following the correlation of the second normal polarity interval to C3An.1n, we propose two options (A and B, Supplementary Fig. S2) for correlating the magnetostratigraphy to the GPTS (Hilgen et al., 2012):

Option A: Continuous sedimentation at 7.1 cm/kyr for the entire section (Fig. 3f, g)

A constant sedimentation rate would lead to an age of 4.77 Ma for the top of the section just below the capping basalt. This agrees well with our $^{40}Ar/^{39}Ar$ ages of 4.95 ± 0.20 Ma (MN12KNG01) and 4.72 ± 0.11 Ma (MN12KNG04; Figs. 2,5). Option A would place the reverse polarity basalt (Platzman et al., 1998) at the top of the section within reverse chron C3n.2r (4.799–4.631 Ma). Option A comes with the inconsistency that normal chron C3n.4n (Thvera) should start at 91.9 m. Three reverse polarity samples, however, occur above 91.9 m (K41.1 and K41.2 at 97.52 m and K42.1 at 99.40 m; Fig. 3e, f).

Option B: The uppermost normal specimen of the section reflects normal polarity chron C3n.4n

Placing the uppermost normal sample at the base of C3n.4n would result in a sedimentation rate of 8.4 cm/kyr for chron C3r. In order to correlate the basalt at the top of the section to chron C3n.2r (according to the newly obtained $^{40}Ar/^{39}Ar$ ages), the sedimentation rate in the unsampled part of the magnetostratigraphic section (104.2 to 125 m) must then be lower (between 3.8 and 5.3 cm/kyr).

For both options A and B we have indicated the interval that correlates to the MSC (Supplementary Fig. S2), as well as its three distinctive stages (PLG, RLG and UG). The onset of the MSC for both options occurs at nearly the same stratigraphic level. Both options imply that continental sedimentation in Lake Kangal spanned the entire Messinian Salinity Crisis, as well as the Miocene-Pliocene boundary. Option B is based on the identification of only one, low-quality single normal polarity specimen. Additionally, the continuous average sedimentation rate of 7.1 cm/kyr of Option A results in an age for the section-covering basalt that perfectly agrees with its reverse polarity and the two newly obtained $^{40}Ar/^{39}Ar$ ages. We therefore prefer option A (Fig. 3f,g).

7.3. *Kangal Basin mammal stratigraphy*

At Kangal 1 (i.e. in laterally equivalent deposits of the sampled Kumarlı section), fossil insectivores, rodents, lagomorpha, carnivores, perissodactyla and proboscidea allow correlation to unit MN13 (Ünay et al., 2003; The NOW Community, 2017). The European Mammal Neogene (MN) Units for the late Miocene are, however, entirely based on Iberian small mammal assemblages (e.g., Hilgen et al., 2012) and may therefore not be readily correlated to Anatolia. Firstly, correlation of the Anatolian small mammal faunas is hindered by the low faunal similarities with well-dated reference localities in Spain. Secondly, the spatio-temporal variation of mammals over larger distances must be taken into account. Additionally, most dispersal events ended in the Iberian Peninsula, as a result of the limited connectivity of the Iberian Peninsula to Africa and Europe (Agusti et al., 2001). According to several authors, an increased connectivity between Africa and Eurasia during the Messinian stage may have led to an exceptional land configuration, resulting in the exchange of African and Iberian fauna (e.g. Benammi et al., 1996; Gibert et al., 2013; García-Alix et al., 2016).

Between the Iberian Peninsula and southeast France, the temporal distribution of rodents has been shown to vary by more than one Myr for the MN zones of the late Tortonian and Messinian (Cano et al., 2011). In contrast to observations on mammal dispersal (Agusti et al., 2001), rodents dispersed earlier in Iberia than in southeast France. Our proposed chronology for the Kangal Basin allows us to correlate the continental sediments to chrons C3An.2n to C3n.2r, which implies that sedimentation occurred during MN13 and well into MN14 and maybe even MN15. Depending on the exact stratigraphic position of the mammal finds at Kangal 1 with respect to the Kumarlı magnetostratigraphic section, this may imply that i) the mammal chronology as defined in Spain can in fact be applied to Turkey, or that, ii) if the mammal finds correlate to the part of the time scale that represents MN14-15 in Spain, the mammal assemblages that represent MN14-15 arrived later in Turkey than in Spain. Our results therefore have direct implications for spatio-temporal variations in the distribution of mammals across Europe and the near East.

7.4. *Records and models of MSC paleoenvironmental change*

Generally, MSC proxy records of paleoenvironmental change fall into three groups:

1) *Records that track changes in Mediterranean and Paratethys basin hydrology.*

Evidence for overspilling of Paratethys into the Mediterranean Basin during the MSC comes from molluscs, dinoflagellates and ostracods with Paratethys affinity that are found within the Mediterranean Basin (e.g. Stoica et al., 2016), whereas hydrogen isotopic (δD) compositions from long-chain alkenones are indicative of periods with a negative water budget in the Mediterranean and Paratethys (Vasiliev et al., 2013, 2015, 2017).

2) *Continental proxy records from brackish-marine Mediterranean and Paratethys basin deposits.*

These proxy data provide information on paleoenvironmental change that occurred directly adjacent to the basins. An example is long-chain *n*-alkanes, which form part of terrestrial plant waxes that were transported into the Mediterranean and Paratethys basins through rivers. Changes in δD values of these long-chain *n*-alkanes document hydrological change at the site of plant growth, and are thus a proxy for changes in continental rainfall. For Eraclea Minoa (Sicily, Italy) $\delta D_{n\text{-alkane}}$ values indicate a shift to more arid and/or warm conditions during MSC stage 3 (Vasiliev et al., 2017). The shift to lower $\delta D_{n\text{-alkane}}$ values observed in the Paratethys Basin during MSC stage 1 (Vasiliev et al., 2013, 2015) may indicate a diminishing local source of *n*-alkanes, therefore increasing the relative contribution of a northern, riverine source of *n*-alkanes (e.g. from the Volga, Dniepr and Don rivers). Overall, positive and negative shifts in $\delta D_{n\text{-alkane}}$ of up to 20–40‰ can be observed in the $\delta D_{n\text{-alkane}}$ records of the Mediterranean and Paratethys basins during the MSC.

3) *Studies identifying paleoenvironmental changes in the Mediterranean and Paratethys during the MSC that directly target the continental Messinian rock record.*

A review of pollen data covering the circum-Mediterranean region reveals that the climatic effects of the MSC were limited, if not absent (Fauquette et al., 2006). Closer to Anatolia, regional vegetation and mammal studies show either virtually no climate change (Gregor and Velitzelos, 1987; Velitzelos and Gregor, 1990; Velitzelos, 1995; Pavlakis, 1999), or drier conditions and increasingly open habitats during the approximate time interval of the MSC, followed by wetter conditions and more forested habitats during the Pliocene (Koufos and Vasileiadou, 2015). None of the studies, however, provide a continuous record through the MSC.

Numerical modeling efforts of the effects of the MSC on circum-Mediterranean climate tested three extreme scenarios with respect to a Tortonian reference simulation (Schneck et al., 2010). These model runs include a sea-level drop of 1500 m with (LOWGRASS) and without (LOWSEA) a replacement of the sea surface by grassland and a complete replacement of the Mediterranean Sea surface by grassland (GRASS). Within the Mediterranean Basin, the effects on temperature are largest (up to +6 °C) in the LOWGRASS model (LOWSEA: up to +2 °C, GRASS: up to +4 °C) as well as on the sum of precipitation minus evaporation (LOWGRASS: up to +700 mm/yr, LOWSEA: up to −200 mm/yr, GRASS: up to +700 mm/yr). The simulated effects of the MSC over Anatolia are, however, limited. Temperature changes in all three models are smaller than ± 2 °C and no changes in precipitation are observed in the LOWSEA and GRASS model runs. The LOWGRASS simulation predicts a 100–200 mm/yr decrease in precipitation. The maximum annual average anomalies of precipitation minus evaporation are −100 mm/yr for all three scenarios, which would suggest a shift to a slightly more negative water balance over Anatolia during the MSC.

To our knowledge, the isotopic data set presented in this study is the only continuous continental record of paleoenvironment in the Mediterranean realm that spans the entire MSC.

7.5. Stable isotope geochemistry of lacustrine carbonates as a proxy for continental paleoenvironmental change

The stable isotopic record of ancient lake systems contains valuable information regarding the paleoenvironmental conditions under which lacustrine carbonates precipitated. The carbon isotopic composition of lake waters ($\delta^{13}C_{lw}$) is mainly controlled by 1) the exchange of CO_2 between the atmosphere and total dissolved inorganic carbon, 2) photosynthesis and respiration of aquatic plants, and 3) the isotopic composition and physicochemical properties of inflowing waters, which in turn are influenced by terrestrial plant respiration and metabolism (e.g. McKenzie, 1985; Kelts and Talbot, 1990; Talbot and Kelts, 1990; Romanek et al., 1992; Leng and Marshall, 2004; Gierlowski-Kordesch, 2010). Differences in fractionation between C4 and C3 plants during carbon fixation lead to $\delta^{13}C$ values approximately 14‰ more positive in C4 than in C3 plants. Conversely, the effect of temperature on carbon fractionation during carbonate precipitation is by comparison relatively small.

The $\delta^{18}O$ values of lake water are largely influenced by the $\delta^{18}O$ values of inflowing water, temperature and lake evaporation. Evaporation and condensation are the principal oxygen isotope fractionation mechanisms for water at the hydrosphere-atmosphere interface (Horita and Wesolowski, 1994). $\delta^{18}O$ values derived from authigenic and biogenic carbonates that formed from lake water are surmised to reflect changes in inflowing water composition and temperature/evaporation (e.g. Leng and Marshall, 2004). The positive covariance between $\delta^{13}C$ and $\delta^{18}O$ values (i.e. maxima in $\delta^{13}C$ occur with maxima in $\delta^{18}O$) in lacustrine carbonates is generally due to productivity changes in closed lakes (e.g. Li and Ku, 1997); higher $\delta^{13}C$ values generally translate to an increase in biogenic productivity, unless there is a shift from C3 to C4 carbon fixation.

7.6. Paleoenvironmental conditions

The Kumarlı section displays a clear positive covariance of $\delta^{13}C$ and $\delta^{18}O$ throughout the sampled section (Supplementary Fig. S1). Higher $\delta^{13}C$ carbonate values likely result from an increase in uptake of ^{12}C by aquatic plants during photosynthesis, and thus reflect an increase in biologic productivity. Higher $\delta^{18}O$ values are best explained by an increase in evaporation, i.e. a more negative lake water balance. We therefore interpret the covariance between $\delta^{13}C$ and $\delta^{18}O$ mainly as an expression of the coupling between lake water balance and biologic productivity, in which periods with a more negative (positive) water balance are characterized by higher (lower) biologic productivity. $\delta^{18}O$ values attaining up to 25‰ in the Kumarlı section are, however, not indicative of strongly evaporative conditions: highly evaporative lake conditions in the Oligocene and late Pleistocene to Holocene CAP interior are typically represented by $\delta^{18}O$ values of up to 36‰ (e.g. Leng et al., 1999; Roberts et al., 2001; Jones et al., 2006, 2007; Lüdecke et al., 2013; Dean et al., 2015).

The basalt that covers the Kumarlı section can be traced over a distance of ~20 km (towards $^{40}Ar/^{39}Ar$ sampling location M12KNG04; Fig. 2b). The absence of deposits on top of the basalt suggests that sedimentation ceased in the Zanclean. The sedimentary rocks and the $\delta^{13}C$ and $\delta^{18}O$ values of the interval directly underlying the basalt provide some information to what may have caused the cessation of lake deposition. The sedimentary logs of the Kumarlı section indicate less detrital input toward the top of the section (> 103 m) which is dominated by white, carbonate-rich units. The $\delta^{18}O$ values in the top interval (Interval 5, 106–121 m in Fig. 9) are overall higher than for the lower part of the section, yet not indicative of extreme lake evaporation. We therefore argue that evaporation caused by an increasingly negative water budget did not cause the demise of Lake Kangal. It is therefore more likely that Lake Kangal was drained by river incision.

7.7. The impact of the MSC on $\delta^{13}C$ and $\delta^{18}O$

Limited connectivity of the Mediterranean Sea to the Atlantic caused episodes of a highly negative water balance in the Mediterranean Sea during MSC stages 2 (RLG) and 3 (UG); Vasiliev et al., 2017). During the peak of the MSC (stage 2, RLG), the Paratethys water budget was strongly negative (Vasiliev et al., 2013). The Mediterranean and Paratethys negative water budgets may have conversely led to an increase in Mediterranean and Paratethys water $\delta^{18}O$ values, as well as an increase in values of $\delta^{18}O$ in atmospheric moisture that eventually reached Anatolia. At first inspection, $\delta^{13}C$ and $\delta^{18}O$ values of the sampled Kumarlı section show relatively low variability and no significant overall shift toward higher or lower values through time, especially at the inferred onset of the MSC (Fig. 9). Consequently, we conclude that the effect of the MSC on the $\delta^{18}O$ values of lacustrine carbonate in Lake Kangal was limited. Following the obtained precise chronology for the Kangal section, we can, however, conclude that the Kumarlı section potentially captures some paleoenvironmental effects of MSC basin dynamics on the Anatolian continental interior. Three observations in the Kumarlı $\delta^{13}C$ record characterize the MSC period (intervals 2 and 3 in Fig. 9): 1) a period of rather stable $\delta^{13}C$ values that average 7.5 ± 0.5‰ (42.6–63.4 m, Interval 2); 2) three positive spikes in lake carbonate $\delta^{13}C$, of which one is coeval with a single-sample spike in $\delta^{18}O$ values (at 80.6 m) and one is coeval with a multiple-sample spike in $\delta^{18}O$ values (64.1–82.3 m, Interval 3). The three episodes of higher lake carbonate $\delta^{13}C$ (at approximately 65 m, 70 m and 80 m; interval 3), all occur in layers with light red clayey limestones (Fig. 9); and 3) a drop in $\delta^{13}C$ to values below −8‰ at the transition to Interval 4.

The positive covariance in $\delta^{13}C$ and $\delta^{18}O$ values of the Kangal section likely reflects a coupling between biologic productivity and the amount of precipitation that reaches central Anatolia, rather than changes in the $\delta^{18}O$ of incoming precipitation (§7.6). The changes in the amount of incoming precipitation that are most strongly displayed in the three peaks in Interval 3 may therefore be linked to specific stages of the MSC. Following the magnetostratigraphic correlation (Fig. 3), we observe that the only peak in $\delta^{13}C$ that is coupled to a multi-sample peak in $\delta^{18}O$ in Interval 3 is closely spaced in time with the acme of the MSC (stage 2, RLG, 50 kyr), and has a similar duration. We therefore surmise that the coupled $\delta^{13}C$-$\delta^{18}O$ peak is in fact an expression of the MSC acme (RLG), which suggests that during extreme lowstand of Mediterranean water levels the amount of incoming precipitation was lower, leading to slightly drier conditions over Anatolia.

The correlation of the magnetostratigraphy to the GPTS places the drop in mean $\delta^{18}O$ values at the start of Interval 4 at the Miocene-Pliocene boundary. Kayseri-Özer (2017) reviewed a large number of climate studies that provide estimates of paleo-MAP, and observed an increase in MAP from the late Miocene into the Pliocene. The lower mean $\delta^{18}O$ values that we observe in Interval 4 (Fig. 9) with respect to the previous intervals (1–3) may therefore reflect the overall increase of MAP into the Pliocene.

To our knowledge, this isotopic data set is the only continuous record of paleoenvironment that spans the entire MSC in the Mediterranean realm. The only correlation of our $\delta^{13}C$-$\delta^{18}O$ record with the MSC can be seen during the RLG. The drop of $\delta^{18}O$ values that follows the Miocene is likely related to an increase in Pliocene rainfall amounts. Overall, we find subtle effects of the MSC on the hydrology and biogenic productivity of Lake Kangal, as expressed in $\delta^{18}O$ and $\delta^{13}C$. By extension, we argue that there was only a limited effect of the MSC on central Anatolian paleoclimate, which is in concordance with other proxy studies (Gregor and Velitzelos, 1987; Velitzelos and Gregor, 1990; Velitzelos, 1995; Pavlakis, 1999) and modeling results (Schneck et al., 2010).

8. Conclusions

The paleomagnetic, magnetostratigraphic, $^{40}Ar/^{39}Ar$, $\delta^{18}O$ and $\delta^{13}C$ results from the sampled Kumarlı section within the Kangal Basin (central Anatolia) reveal that:

- ○ The 125 m long, fluvio-lacustrine Kumarlı section covers ca. 1.8 Myrs, from ca. 6.6 Ma to ca. 4.8 Ma, at an average sedimentation rate of 7.1 cm/kyr, and is covered by a basalt dated at 4.95 ± 0.20 Ma and 4.72 ± 0.11 Ma. The section therefore covers the entire period of the Messinian Salinity Crisis (MSC) and the Miocene-Pliocene boundary. It is, to our knowledge, the only continuous continental MSC section within the Mediterranean realm.
- ○ The $\delta^{13}C$ and $\delta^{18}O$ results (n = 101) of the sampled fluvio-lacustrine carbonates yield mean values of −7.6 ± 0.9‰ and 23.0 ± 1.1‰, respectively. The low 1σ standard deviations indicate no large changes in $\delta^{13}C$ and $\delta^{18}O$ throughout the section. We observe a covariance between $\delta^{13}C$ and $\delta^{18}O$. We therefore interpret changes in $\delta^{13}C$ and $\delta^{18}O$ to reflect changes in the amount of precipitation that reached central Anatolia, rather than changes in the $\delta^{18}O$ of incoming precipitation.
- ○ The period of the MSC had a profound impact on the climatic conditions (precipitation, temperature) within the Mediterranean and Paratethys basins. In contrast, the Kumarlı $\delta^{13}C$ and $\delta^{18}O$ values show overall subtle changes and variability during the MSC, and the MSC therefore had limited impact on the paleoclimatic and paleoenvironmental conditions of central Anatolia. The largest, coupled peak in $\delta^{18}O$ and $\delta^{13}C$, however, occurred during the acme of the MSC (Stage 2, Resedimented Lower Gypsum). We therefore suggest that during extreme lowstand of the Mediterranean the amount of incoming precipitation was lower, leading to slightly drier conditions over Anatolia. The 1‰ drop in $\delta^{18}O$ values at the end of the MSC most likely reflects a distinct increase in MAP, which is also observed in proxy studies across the Miocene-Pliocene boundary.
- ○ The basalt that caps the section is stratigraphically at the highest position within the late Miocene to Pliocene fluvio-lacustrine Kangal Basin. $\delta^{18}O$ values up to ~25‰ are not indicative of evaporative conditions, and we therefore suggest that the demise of Lake Kangal (~150 km × 30 km) was caused by river incision.
- ○ The late Miocene mammal chronology is entirely based on Iberian mammal assemblages. Nevertheless, the proposed age of the sedimentary rocks of the sampled interval based on mammal stratigraphy (MN13, i.e. 7.4/6.8–5.3 Ma; Hilgen et al., 2012) accords well with the newly established magnetostratigraphy.

Supplementary data to this article can be found online at https://doi.org/10.1016/j.palaeo.2018.03.001.

Acknowledgements

We acknowledge support through the NSF Continental Dynamics program (EAR-1109762) “Central Anatolian Tectonics (CD-CAT)” to Whitney; the College of Science and Engineering, University of Minnesota (Meijers), and the LOEWE initiative of Hesse's Ministry of Higher Education, Research, and the Arts (Mulch). We thank Mary Reid for sampling of the basalt; Ömer Balak for conducting paleomagnetic lab work; Côme Lefebvre, Seçkin Şiş and Levent Tosun for their help in the field; Jens Fiebig for laboratory support at the joint Goethe University—Senckenberg BiK-F Stable Isotope Facility; satellite imagery copyright by DigitalGlobe, Inc., provided through the Polar Geospatial Center (University of Minnesota—Twin Cities) and processed by Côme Lefebvre; Iuliana Vasiliev for discussion; Faruk Ocakoğlu and an anonymous reviewer for their constructive reviews, as well as Ferhat Kaya for conducting the mandatory internal UGSG review. Any use of trade, product, or firm names is for descriptive purposes only and does not imply endorsement by the U.S. Government.

References

Agusti, J., Cabrera, L., Garcés, M., Krijgsman, W., Oms, O., Parés, J.M., 2001. A calibrated mammal scale for the Neogene of Western Europe. State of the art. Earth Sci. Rev. 52 (4), 247–260.

Akgün, F., Kayseri, M.S., Akkiraz, M.S., 2007. Palaeoclimatic evolution and vegetational changes during the Late Oligocene–Miocene period in Western and Central Anatolia (Turkey). Palaeogeogr. Palaeoclimatol. Palaeoecol. 253 (1), 56–90.

Akkiraz, M.S., Akgün, F., Utescher, T., Bruch, A.A., Mosbrugger, V., 2011. Precipitation gradients during the Miocene in Western and Central Turkey as quantified from pollen data. Palaeogeogr. Palaeoclimatol. Palaeoecol. 304 (3), 276–290.

Aydar, E., Schmitt, A.K., Çubukçu, H.E., Akin, L., Ersoy, O., Sen, E., Duncan, R.A., Atici, G., 2012. Correlation of ignimbrites in the central Anatolian volcanic province using zircon and plagioclase ages and zircon compositions. J. Volcanol. Geotherm. Res. 213, 83–97.

Bahr, A., Kaboth, S., Jiménez-Espejo, F.J., Sierro, F.J., Voelker, A.H.L., Lourens, L., Röhl, U., Reichart, G.J., Escutia, C., Hernández-Molina, F.J., Pross, J., 2015. Persistent monsoonal forcing of Mediterranean Outflow Water dynamics during the late Pleistocene. Geology 43 (11), 951–954.

Benammi, M., Calvo, M., Prévot, M., Jaeger, J.J., 1996. Magnetostratigraphy and paleontology of Aït Kandoula basin (High Atlas, Morocco) and the African-European late Miocene terrestrial fauna exchanges. Earth Planet. Sci. Lett. 145 (1), 15–29.

Bosma, A.A., Bruijn, H.D., Wessels, W., 2013. Late Miocene Sciuridae (Mammalia, Rodentia) from Anatolia, Turkey. J. Vertebr. Paleontol. 33 (4), 924–942.

Butler, R.F., 1992. Paleomagnetism: Magnetic Domains to Geologic Terranes. vol. 319 Blackwell Scientific Publications, Boston.

Cano, A.R.G., Fernández, M.H., Álvarez-Sierra, M.Á., 2011. Biogeographic provincialism in rodent faunas from the Iberoccitanian Region (southwestern Europe) generates severe diachrony within the Mammalian Neogene (MN) biochronologic scale during the Late Miocene. Palaeogeogr. Palaeoclimatol. Palaeoecol. 307 (1), 193–204.

Cosentino, D., Schildgen, T.F., Cipollari, P., Faranda, C., Gliozzi, E., Hudáčková, N., Lucifora, S., Strecker, M.R., 2012. Late Miocene surface uplift of the southern margin of the Central Anatolian Plateau, Central Taurides, Turkey. Geol. Soc. Am. Bull. 124 (1–2), 133–145.

Dalrymple, G.B., Alexander, E.C., Lanphere, M.A., Kraker, G.P., 1981. Irradiation of samples for ^{40}Ar/^{39}Ar dating using the Geological Survey TRIGA reactor (No. 1176). USGPO.

Dean, J.R., Jones, M.D., Leng, M.J., Sloane, H.J., Roberts, C.N., Woodbridge, J., Swann, G.E., Metcalfe, S.E., Eastwood, W.J., Yiğitbaşıoğlu, H., 2013. Palaeo-seasonality of the last two millennia reconstructed from the oxygen isotope composition of carbonates and diatom silica from Nar Gölü, central Turkey. Quat. Sci. Rev. 66, 35–44.

Dean, J.R., Jones, M.D., Leng, M.J., Noble, S.R., Metcalfe, S.E., Sloane, H.J., Sahy, D., Eastwood, W.J., Roberts, C.N., 2015. Eastern Mediterranean hydroclimate over the late glacial and Holocene, reconstructed from the sediments of Nar lake, central Turkey, using stable isotopes and carbonate mineralogy. Quat. Sci. Rev. 124, 162–174.

Deenen, M.H., Langereis, C.G., van Hinsbergen, D.J., Biggin, A.J., 2011. Geomagnetic secular variation and the statistics of palaeomagnetic directions. Geophys. J. Int. 186 (2), 509–520.

Deenen, M.H.L., Langereis, C.G., Van Hinsbergen, D.J.J., Biggin, A.J., 2014. Erratum to Geomagnetic secular variation and the statistics of palaeomagnetic directions. Geophys. J. Int. 186 (2011), 509–520 (Geophysical Journal International. 197(1), pp. 643).

Fauquette, S., Suc, J.P., Bertini, A., Popescu, S.M., Warny, S., Taoufiq, N.B., Villa, M.J.P., Chikhi, H., Feddi, N., Subally, D., Clauzon, G., 2006. How much did climate force the Messinian salinity crisis? Quantified climatic conditions from pollen records in the Mediterranean region. Palaeogeogr. Palaeoclimatol. Palaeoecol. 238 (1), 281–301.

Fisher, R., 1953. Dispersion on a sphere. In: Proceedings of the Royal Society of London A: Mathematical, Physical and Engineering Sciences. vol. 217, No. 1130. The Royal Society, pp. 295–305.

Flecker, R., Krijgsman, W., Capella, W., de Castro Martíns, C., Dmitrieva, E., Mayser, J.P., Marzocchi, A., Modestou, S., Ochoa, D., Simon, D., Tulbure, M., 2015. Evolution of the Late Miocene Mediterranean–Atlantic gateways and their impact on regional and global environmental change. Earth Sci. Rev. 150, 365–392. http://dx.doi.org/10.1016/j.earscirev.2015.08.007.

García-Alix, A., Minwer-Barakat, R., Martín Suárez, E., Freudenthal, M., Aguirre, J., Kaya, F., 2016. Updating the Europe–Africa small mammal exchange during the late Messinian. J. Biogeogr. 43 (7), 1336–1348.

Gibert, L., Scott, G.R., Montoya, P., Ruiz-Sánchez, F.J., Morales, J., Luque, L., Abella, J., Lería, M., 2013. Evidence for an African-Iberian mammal dispersal during the pre-evaporitic Messinian. Geology 41 (6), 691–694.

Gierlowski-Kordesch, E.H., 2010. Lacustrine carbonates. Dev. Sedimentol. 61, 1–101.

Gregor, H.J., Velitzelos, E., 1987. Evolution of Neogene Mediterranean vegetation and the question of a dry upper Miocene period (salinity crisis). Bull. Inst. Geol. Publ. Hung. 70, 489–496.

Gürsoy, H., Piper, J.D.A., Tatar, O., Temiz, H., 1997. A palaeomagnetic study of the Sivas Basin, central Turkey: crustal deformation during lateral extrusion of the Anatolian Block. Tectonophysics 271 (1), 89–105.

Gürsoy, H., Tatar, O., Piper, J.D.A., Koçbulut, F., Akpınar, Z., Huang, B., Roberts, A.P., Mesci, B.L., 2011. Palaeomagnetic study of the Kepezdağ and Yamadağ volcanic complexes, central Turkey: Neogene tectonic escape and block definition in the central-east Anatolides. J. Geodyn. 51 (5), 308–326.

Hilgen, F.J., Lourens, L.J., Van Dam, J.A., Beu, A.G., Boyes, A.F., Cooper, R.A., Krijgsman, W., Ogg, J.G., Piller, W.E., Wilson, D.S., 2012. Chapter 29 - The Neogene Period. In: Gradstein, F.M., Ogg, J.G., Schmitz, M.D., Ogg, G.M. (Eds.), The Geologic Time Scale. Elsevier, Boston, pp. 923–978. http://dx.doi.org/10.1016/B978-0-444-59425-9.00029-9.

Hopkinson, J., 1989. Magnetic and other physical properties of iron at a high temperature. Philos. Trans. R. Soc. Lond. A 180, 443.

Horita, J., Wesolowski, D.J., 1994. Liquid-vapor fractionation of oxygen and hydrogen isotopes of water from the freezing to the critical temperature. Geochim. Cosmochim. Acta 58 (16), 3425–3437.

Hsü, K.J., Ryan, W.B.F., Cita, M.B., 1973. Late Miocene desiccation of the Mediterranean. Nature 242 (5395), 240–244.

Ivanovic, R.F., Valdes, P.J., Flecker, R., Gutjahr, M., 2014. Modelling global-scale climate impacts of the late Miocene Messinian Salinity Crisis. Clim. Past 10 (2), 607–622.

Jaffey, N., Robertson, A.H., 2001. New sedimentological and structural data from the Ecemiş Fault Zone, southern Turkey: implications for its timing and offset and the Cenozoic tectonic escape of Anatolia. J. Geol. Soc. 158 (2), 367–378.

Jones, M.D., Roberts, C.N., Leng, M.J., Türkeş, M., 2006. A high-resolution late Holocene lake isotope record from Turkey and links to North Atlantic and monsoon climate. Geology 34 (5), 361–364.

Jones, M.D., Roberts, C.N., Leng, M.J., 2007. Quantifying climatic change through the last glacial–interglacial transition based on lake isotope palaeohydrology from central Turkey. Quat. Res. 67 (3), 463–473.

Kaya, F., Kaymakçı, N., 2013. Systematics and dental microwear of the late Miocene Gliridae (Rodentia, Mammalia) from Hayranlı, Anatolia: implications for paleoecology and paleobiodiversity. Palaeontol. Electron. 16 (3), 1–22.

Kaya, F., Bibi, F., Žliobaitė, I., Eronen, J.T., Hui, T., Fortelius, M., 2018. The rise and fall of the Old World savannah fauna and the origins of the African savannah biome. Nat. Ecol. Evol. 241–246. http://dx.doi.org/10.1038/s41559-017-0414-1.

Kaymakci, N., Özçelik, Y., White, S.H., Van Dijk, P.M., 2009. Tectono-stratigraphy of the Çankırı Basin: Late Cretaceous to early Miocene evolution of the Neotethyan suture zone in Turkey. In: Van Hinsbergen, D.J.J., Edwards, M.A., Govers, R. (Eds.), Collision and Collapse at the Africa-Arabia-Eurasia Subduction Zone. Geol. Soc. of London, London, pp. 67–106.

Kayseri-Özer, M.S., 2017. Cenozoic vegetation and climate change in Anatolia—a study based on the IPR-vegetation analysis. Palaeogeogr. Palaeoclimatol. Palaeoecol. 467, 37–68.

Kelts, K., Talbot, M., 1990. Lacustrine carbonates as geochemical archives of environmental change and biotic/abiotic interactions. In: Large Lakes. Springer, Berlin Heidelberg, pp. 288–315.

Kirschvink, J.L., 1980. The least-squares line and plane and the analysis of palaeomagnetic data. Geophys. J. Int. 62 (3), 699–718.

Koçyiğit, A., Beyhan, A., 1998. A new intracontinental transcurrent structure: the Central Anatolian Fault Zone, Turkey. Tectonophysics 284, 317–336.

Koufos, G.D., Vasileiadou, K., 2015. Miocene/Pliocene mammal faunas of southern Balkans: implications for biostratigraphy and palaeoecology. Palaeobiodivers. Palaeoenviron. 95 (3), 285–303. http://dx.doi.org/10.1007/s12549-015-0201-4.

Kouwenhoven, T.J., Hilgen, F.J., van der Zwaan, G.J., 2003. Late Tortonian-early Messinian stepwise disruption of the Mediterranean-Atlantic connections: constraints from benthic foraminiferal and geochemical data. Palaeogeogr. Palaeoclimatol. Palaeoecol. 198, 303–319.

Koymans, M.R., Langereis, C.G., Pastor-Galan, D., van Hinsbergen, D.J.J., 2016. Paleomagnetism.org: an online multi-platform open source environment for paleomagnetic data analysis. Comput. Geosci. 93, 127–137.

Krijgsman, W., Gaboardi, S., Hilgen, F.J., Iaccarino, S., Kaenel, E.D., Laan, E.V.D., 2004. Revised astrochronology for the Ain el Beida section (Atlantic Morocco): no glacio-eustatic control for the onset of the Messinian Salinity Crisis. Stratigraphy 1, 87–101.

Krijgsman, W., Stoica, M., Vasiliev, I., Popov, V.V., 2010. Rise and fall of the Paratethys Sea during the Messinian Salinity Crisis. Earth Planet. Sci. Lett. 290 (1), 183–191.

Kuiper, K.F., Deino, A., Hilgen, F.J., Krijgsman, W., Renne, P.R., Wijbrans, J.R., 2008. Synchronizing rock clocks of Earth history. Science 320 (5875), 500–504.

Lee, J.-Y., Marti, K., Severinghaus, J.P., Kawamura, K., Yoo, H.-S., Lee, J.B., Kim, J.S., 2006. A redetermination of the isotopic abundances of atmospheric Ar. Geochim. Cosmochim. Acta 70, 4507–4512. http://dx.doi.org/10.1016/j.gca.2006.06.1563.

Leng, M.J., Marshall, J.D., 2004. Palaeoclimate interpretation of stable isotope data from lake sediment archives. Quat. Sci. Rev. 23 (7), 811–831.

Leng, M.J., Roberts, N., Reed, J.M., Sloane, H.J., 1999. Late Quaternary palaeohydrology of the Konya Basin, Turkey, based on isotope studies of modern hydrology and lacustrine carbonates. J. Paleolimnol. 22 (2), 187–204.

Li, H.C., Ku, T.L., 1997. δ^{13}C–δ^{18}C covariance as a paleohydrological indicator for closed-basin lakes. Palaeogeogr. Palaeoclimatol. Palaeoecol. 133 (1–2), 69–80.

Lüdecke, T., Mikes, T., Rojay, F.B., Cosca, M.A., Mulch, A., 2013. Stable isotope-based reconstruction of Oligo-Miocene paleoenvironment and paleohydrology of Central Anatolian lake basins (Turkey). Turk. J. Earth Sci. 22 (5), 793–819. http://dx.doi.org/10.3906/yer-1207-11.

Marzocchi, A., Lunt, D.J., Flecker, R., Bradshaw, C.D., Farnsworth, A., Hilgen, F.J., 2015. Orbital control on late Miocene climate and the North African monsoon: insight from an ensemble of sub-precessional simulations. Clim. Past 11 (10), 1271–1295.

Mazzini, I., Hudackova, N., Joniak, P., Kovacova, M., Mikes, T., Mulch, A., Rojay, F.B., Lucifora, S., Esu, D., Soulie-Marsche, I., 2013. Palaeoenvironmental and chronological constraints on the Tuglu Formation (Cankırı Basin, Central Anatolia, Turkey). Turk. J. Earth Sci. 22 (5), 747–777. http://dx.doi.org/10.3906/yer-1207-10.

McKenzie, J.A., 1985. Carbon isotopes and productivity in the lacustrine and marine environment. In: Chemical Processes in Lakes. 1985. John Wiley and Sons, New York New York, pp. 99–118.

Meijers, M.J.M., Kaymakçı, N., van Hinsbergen, D.J.J., Langereis, C.G., Stephenson, R.A., Hippolyte, J.-C., 2010. Late Cretaceous to Paleocene oroclinal bending in the central Pontides (Turkey). Tectonics 29. http://dx.doi.org/10.1029/2009TC002620.

Min, K., Mundil, R., Renne, P.R., Ludwig, K.R., 2000. A test for systematic errors ^{40}Ar/^{39}Ar geochronology through comparison with U/Pb analysis of a 1.1-Ga rhyolite. Geochim. Cosmochim. Acta 64, 73–98. http://dx.doi.org/10.1016/S0016-7037(99)00204-5.

Ocakoğlu, F., Yavuz, N., Aydın, A., Yılmaz, İ.Ö., 2018. Orbitally-driven Mid-Burdigalian Coastal Sabkha cycles from the Sivas Basin: sedimentological, paleontological, and geochemical data. Palaeogeogr. Palaeoclimatol. Palaeoecol. 490, 505–521.

Özsayin, E., Ciner, T.A., Rojay, F.B., Dirik, R.K., Melnick, D., Fernandez-Blanco, D., 2014. Plio-Quaternary extensional tectonics of the Central Anatolian Plateau: a case study from the Tuz Gölü Basin, Turkey. Turk. J. Earth Sci. 22, 691–714.

Pastor-Galán, D., Mulchrone, K.F., Koymans, M.R., van Hinsbergen, D.J.J., Langereis, C.G., 2017. Bootstrapped Total Least Squares orocline test: a robust method to quantify vertical axis rotation patterns in orogens, with examples from the Cantabrian and Aegean oroclines. Lithosphere. http://dx.doi.org/10.1130/L547.1.

Pavlakis, P., 1999. The Messinian events and the Greek fossil mammal record. Deinsea 7 (1), 233–252.

Platzman, E.S., Tapirdamaz, C., Sanver, M., 1998. Neogene anticlockwise rotation of central Anatolia (Turkey): preliminary palaeomagnetic and geochronological results.

Tectonophysics 299 (1), 175–189.

Poisson, A., Vrielynck, B., Wernli, R., Negri, A., Bassetti, M.A., Büyükmeriç, Y., Özer, S., Guillou, H., Kavak, K.S., Temiz, H., Orszag-Sperber, F., 2016. Miocene transgression in the central and eastern parts of the Sivas Basin (Central Anatolia, Turkey) and the Cenozoic palaeogeographical evolution. Int. J. Earth Sci. 105 (1), 339–368.

Popov, S.V., Shcherba, I.G., Ilyina, L.B., Nevesskaya, L.A., Paramonova, N.P., Khondkarian, S.O., Magyar, I., 2006. Late Miocene to Pliocene palaeogeography of the Paratethys and its relation to the Mediterranean. Palaeogeogr. Palaeoclimatol. Palaeoecol. 238 (1), 91–106.

Roberts, N., Reed, J.M., Leng, M.J., Kuzucuoğlu, C., Fontugne, M., Bertaux, J., Woldring, H., Bottema, S., Black, S., Hunt, E., Karabiyikoğlu, M., 2001. The tempo of Holocene climatic change in the eastern Mediterranean region: new high-resolution crater-lake sediment data from central Turkey. The Holocene 11 (6), 721–736.

Rohling, E.J., Marino, G., Grant, K.M., 2015. Mediterranean climate and oceanography, and the periodic development of anoxic events (sapropels). Earth Sci. Rev. 143, 62–97. http://dx.doi.org/10.1016/j.earscirev.2015.01.008.

Romanek, C.S., Grossman, E.L., Morse, J.W., 1992. Carbon isotopic fractionation in synthetic aragonite and calcite: effects of temperature and precipitation rate. Geochim. Cosmochim. Acta 56 (1), 419–430.

Rouchy, J.M., Caruso, A., 2006. The Messinian salinity crisis in the Mediterranean basin: a reassessment of the data and an integrated scenario. Sediment. Geol. 188, 35–67.

Roveri, M., Lugli, S., Manzi, V., Schreiber, B.C., 2008. The Messinian Sicilian stratigraphy revisited: new insights for the Messinian salinity crisis. Terra Nova 20 (6), 483–488.

Roveri, M., Flecker, R., Krijgsman, W., Lofi, J., Lugli, S., Manzi, V., Sierro, F.J., Bertini, A., Camerlenghi, A., De Lange, G., Govers, R., 2014. The Messinian Salinity Crisis: past and future of a great challenge for marine sciences. Mar. Geol. 352, 25–58.

Schemmel, F., Mikes, T., Rojay, B., Mulch, A., 2013. The impact of topography on isotopes in precipitation across the Central Anatolian Plateau (Turkey). Am. J. Sci. 313 (2), 61–80.

Schneck, R., Micheels, A., Mosbrugger, V., 2010. Climate modelling sensitivity experiments for the Messinian Salinity Crisis. Palaeogeogr. Palaeoclimatol. Palaeoecol. 286 (3), 149–163.

Şengör, A.M.C., Yilmaz, Y., 1981. Tethyan evolution of Turkey: a plate tectonic approach. Tectonophysics 75 (3–4), 181–241.

Şengör, A.M.C., Görür, N., Şaroğlu, F., 1985. Strike-slip faulting and related basin formation in zones of tectonic escape: Turkey as a case study. In: Bıddle, K.T., Chrıstıe-Blıck, N. (Eds.), Strike-Slip Faulting and Basin Formation. Society of Economic Paleontologists and Mineralogists, Special Publications 37. pp. 227–264.

Sierro, F.J., Hilgen, F.J., Krijgsman, W., Flores, J.A., 2001. The Abad composite (SE Spain): a Messinian reference section for the Mediterranean and the APTS. Palaeogeogr. Palaeoclimatol. Palaeoecol. 168 (1), 141–169.

Spötl, C., Vennemann, T.W., 2003. Continuous-flow isotope ratio mass spectrometric analysis of carbonate minerals. Rapid Commun. Mass Spectrom. 17 (9), 1004–1006.

Stoica, M., Krijgsman, W., Fortuin, A., Gliozzi, E., 2016. Paratethyan ostracods in the Spanish Lago-Mare: more evidence for interbasinal exchange at high Mediterranean sea level. Palaeogeogr. Palaeoclimatol. Palaeoecol. 441, 854–870.

Strömberg, C.A., Werdelin, L., Friis, E.M., Saraç, G., 2007. The spread of grass-dominated habitats in Turkey and surrounding areas during the Cenozoic: phytolith evidence. Palaeogeogr. Palaeoclimatol. Palaeoecol. 250 (1), 18–49.

Talbot, M.R., Kelts, K., 1990. Paleolimnological Signatures from Carbon and Oxygen Isotopic Ratios in Carbonates, from Organic Carbon-Rich Lacustrine Sediments. (Chapter 6).

Tauxe, L., 2010. Essentials of paleomagnetism. Univ of California Press.

The NOW Community, 2017. New and Old Worlds Database of Fossil Mammals (NOW). Licensed under CC BY 4.0. Release, retrieved June 21, 2017 from. http://www.helsinki.fi/science/now/.

Torsvik, T.H., Van der Voo, R., Preeden, U., Mac Niocaill, C., Steinberger, B., Doubrovine, P.V., van Hinsbergen, D.J., Domeier, M., Gaina, C., Tohver, E., Meert, J.G., 2012. Phanerozoic polar wander, palaeogeography and dynamics. Earth Sci. Rev. 114 (3), 325–368.

Umhoefer, P.J., Whitney, D.L., Teyssier, C., Fayon, A.K., Casale, G., Heizler, M.T., 2007. Yo-yo tectonics in a wrench zone, Central Anatolian fault zone, Turkey. Geol. Soc. Am. Spec. Pap. 434, 35–57.

Ünay, E., De Bruijn, H., Saraç, G., 2003. A preliminary zonation of the continental Neogene of Anatolia based on rodents. Deinsea 10 (35), 539–548.

Van der Laan, E., Gaboardi, S., Hilgen, F.J., Lourens, L.J., 2005. Regional climate and glacial control on high-resolution oxygen isotope records from Ain el Beida (latest Miocene, northwest Morocco): a cyclostratigraphic analysis in the depth and time domain. Paleoceanography 20 (1).

Vasiliev, I., Reichart, G.J., Krijgsman, W., 2013. Impact of the Messinian Salinity Crisis on Black Sea hydrology—insights from hydrogen isotopes analysis on biomarkers. Earth Planet. Sci. Lett. 362, 272–282.

Vasiliev, I., Reichart, G.J., Grothe, A., Damsté, J.S.S., Krijgsman, W., Sangiorgi, F., Weijers, J.W., van Roij, L., 2015. Recurrent phases of drought in the upper Miocene of the Black Sea region. Palaeogeogr. Palaeoclimatol. Palaeoecol. 423, 18–31.

Vasiliev, I., Mezger, E.M., Lugli, S., Reichart, G.J., Manzi, V., Roveri, M., 2017. How dry was the Mediterranean during the Messinian salinity crisis? Palaeogeogr. Palaeoclimatol. Palaeoecol. 471, 120–133.

Velitzelos, E., 1995. The effects of the Mediterranean Messinian Salinity Crisis on the Neogene Floras of Greece. In: International Conference on the Biotic and Climatic Effects of the Messinian Event on the circum Mediterranean. Technical Programme and Abstractspp. 66.

Velitzelos, E., Gregor, H.J., 1990. Some aspects of the Neogene floral history in Greece. Rev. Palaeobot. Palynol. 62 (3–4), 291–307.

Velzen, A.V., Zijderveld, J.D.A., 1995. Effects of weathering on single-domain magnetite in Early Pliocene marine marls. Geophys. J. Int. 121 (1), 267–278.

Wilson, M., Tankut, A., Guleç, N., 1997. Tertiary volcanism of the Galatia province, northwest Central Anatolia, Turkey. Lithos 42 (1), 105–121.

Yıldırım, C., Schildgen, T.F., Echtler, H., Melnick, D., Strecker, M.R., 2011. Late Neogene and active orogenic uplift in the Central Pontides associated with the North Anatolian Fault: implications for the northern margin of the Central Anatolian Plateau, Turkey. Tectonics 30 (5).

Zachos, J., Pagani, M., Sloan, L., Thomas, E., Billups, K., 2001. Trends, rhythms, and aberrations in global climate 65 Ma to present. Science 292 (5517), 686–693.

Zhang, Z., Ramstein, G., Schuster, M., Li, C., Contoux, C., Yan, Q., 2014. Aridification of the Sahara desert caused by Tethys Sea shrinkage during the Late Miocene. Nature 513 (7518), 401.

Zijderveld, J.D.A., 1967. AC demagnetization of rocks: analysis of results. In: Collinson, D.W., Creer, K.M., Runcorn, S.K. (Eds.), Methods in Paleomagnetism, pp. 254–286.